

# Measure Transport with Kernel Stein Discrepancy

Matthew A. Fisher<sup>1</sup>, Tui Nolan<sup>2,3</sup>, Matthew M. Graham<sup>1,4</sup>,  
Dennis Prangle<sup>1</sup>, Chris. J. Oates<sup>1,4</sup>

<sup>1</sup>Newcastle University, UK

<sup>2</sup>Cornell University, US

<sup>3</sup>University of Technology Sydney, Australia

<sup>4</sup>Alan Turing Institute, UK

July 17, 2021

## Abstract

Measure transport underpins several recent algorithms for posterior approximation in the Bayesian context, wherein a transport map is sought to minimise the Kullback–Leibler divergence (KLD) from the posterior to the approximation. The KLD is a strong mode of convergence, requiring absolute continuity of measures and placing restrictions on which transport maps can be permitted. Here we propose to minimise a kernel Stein discrepancy (KSD) instead, requiring only that the set of transport maps is dense in an  $L^2$  sense and demonstrating how this condition can be validated. The consistency of the associated posterior approximation is established and empirical results suggest that KSD is competitive and more flexible alternative to KLD for measure transport.

## 1 Introduction

A popular and constructive approach to approximation of complicated distributions is to learn a transformation from a simpler reference distribution. Within machine learning, neural networks are often used to provide flexible families of transformations which can be optimised by stochastic gradient descent on a suitable objective, with *variational autoencoders* [Kingma and Welling, 2013, Rezende et al., 2014], *generative adversarial networks* [Goodfellow et al., 2014], *generative moment matching networks* [Li et al., 2015, Dziugaite et al., 2015] and *normalizing flows* [Rezende and Mohamed, 2015, Kingma et al., 2016, Dinh et al., 2016, Papamakarios et al., 2019, Kobyzev et al., 2020] all fitting in this framework. The principal application for such generative models is *distribution estimation*; samples are provided from the target distribution and the task is to fit a distribution to these samples.

Parallel developments within applied mathematics view the transformation as a *transport map* performing *measure transport* [Marzouk et al., 2016, Parno and Marzouk, 2018].

The principal application for measure transport is *posterior approximation*; an un-normalised density function defines the complicated distribution and the task is to approximate it. In this paper we study posterior approximation, noting that the flexible transformations developed in the machine learning literature can also be applied to this task.

Measure transport provides a powerful computational tool for Bayesian inference in settings that can be challenging for standard approaches, such as Markov chain Monte Carlo (MCMC) or mean field variational inference. For example, even sophisticated MCMC methods can fail when a posterior is concentrated around a sub-manifold of the parameter space [Livingstone and Zanella, 2019, Au et al., 2020], while it can be relatively straight-forward to define a transport map whose image is the sub-manifold [Parno and Marzouk, 2018, Brehmer and Cranmer, 2020]. Likewise, mean field variational inference methods can perform poorly in this context, since independence assumptions can be strongly violated [Blei et al., 2017].

Let  $\mathcal{Y}$  be a measurable space equipped with a probability measure  $P$ , representing the posterior to be approximated. The task that we consider in this paper is to elicit a second measurable space  $\mathcal{X}$ , equipped with a probability measure  $Q$ , and a measurable function  $T : \mathcal{X} \rightarrow \mathcal{Y}$ , such that the push-forward  $T_{\#}Q$  (i.e. the measure produced by applying  $T$  to samples from  $Q$ ) approximates  $P$ , in a sense to be specified.

It is further desired that  $Q$  should be a “simple” distribution that is easily sampled. In contrast to the literature on normalising flows, it is *not* stipulated that  $T$  should be a bijection, since we wish to allow for situations where  $\mathcal{X}$  and  $\mathcal{Y}$  have different cardinalities or where  $P$  is supported on a sub-manifold.

A natural starting point is a notion of *discrepancy*  $\mathcal{D}(P_1, P_2)$  between two probability measures,  $P_1$  and  $P_2$ , on  $\mathcal{Y}$ , with the property that  $\mathcal{D}(P_1, P_2) = 0$  if and only if  $P_1$  and  $P_2$  are equal.

Then one selects a measurable space  $\mathcal{X}$  and associated probability measure  $Q$  and seeks a solution to

$$\arg \min_{T \in \mathcal{T}} \mathcal{D}(P, T_{\#}Q), \quad (1)$$

over a suitable set  $\mathcal{T}$  of measurable functions from  $\mathcal{X}$  to  $\mathcal{Y}$ . A popular choice of  $\mathcal{D}$  is the Kullback-Leibler divergence (KLD), giving rise to *variational inference* [Blei et al., 2017], but other discrepancies can be considered [Ranganath et al., 2016]. The problem in (1) can be augmented to include also the selection of  $\mathcal{X}$  and  $Q$ , if desired.

The solution of (1) provides an approximation to  $P$  whose quality will depend on the set  $\mathcal{T}$  and the discrepancy  $\mathcal{D}$ . This motivates us to consider the choice of  $\mathcal{T}$  and  $\mathcal{D}$ , taking into account considerations that go beyond computational tractability. For example, a desirable property would be that, for a sequence of probability measures  $(P_n)_{n \in \mathbb{N}}$ , if  $\mathcal{D}(P, P_n) \rightarrow 0$  then  $P_n \rightarrow P$  in some suitable sense. For  $\mathcal{D} = \mathcal{D}_{\text{KL}}$ , the KLD<sup>1</sup>, it holds that  $\mathcal{D}_{\text{KL}}(P, P_n) \rightarrow 0$  implies  $P_n$  converges to  $P$  in *total variation*, from Pinsker’s inequality [Tsybakov, 2009]. This is a strong mode of convergence, requiring absolute continuity of measures that may be difficult to ensure when the posterior is concentrated near to a sub-manifold. Accordingly, the use of KLD for measure transport places strong and potentially impractical restrictions

---

<sup>1</sup>We use the notation  $\mathcal{D}_{\text{KL}}(P, Q) := \text{KL}(Q||P)$ .

on which maps  $T$  are permitted [e.g. Marzouk et al., 2016, Parno and Marzouk, 2018, required that  $T$  is a diffeomorphism with  $\det \nabla T > 0$  on  $\mathcal{X}$ ]. This motivates us in this paper to consider the use of an alternative discrepancy  $\mathcal{D}$ , corresponding to a weaker mode of convergence, for posterior approximation using measure transport. The advantage of discrepancy measures inducing weaker modes of convergence has also motivated recent developments in generative adversarial networks [Arjovsky et al., 2017].

Our contributions are as follows:

- We propose kernel Stein discrepancy (KSD) as an alternative to KLD for posterior approximation using measure transport, showing that KSD renders (1) tractable for standard stochastic optimisation methods (Proposition 1).
- Using properties of KSD we are able to establish consistency under explicit and verifiable assumptions on  $P$ ,  $Q$  and  $\mathcal{T}$  (Theorem 2).
- Our theoretical assumptions are weak – we do not even require  $T$  to be a bijection – and are verified for a particular class of neural network (Proposition 3). In particular, we do not require  $Q$  and  $P$  to be defined on the same space, allowing quite flexible mappings  $T$  to be constructed.
- Empirical results support KSD as a competitive alternative to KLD for measure transport.

Earlier work on this topic appears limited to Hu et al. [2018], who trained a neural network with KSD. Here we consider general transport maps and we establish consistency of the method, which these earlier authors did not. We note also that gradient flows provide an alternative (implicit) approach to measure transport [Liu and Wang, 2016].

**Outline:** The remainder of the paper is structured as follows: Section 2 introduces measure transport using KSD, Section 3 contains theoretical analysis for this new method, Section 4 presents a detailed empirical assessment and Section 5 contains a discussion of our main findings.

## 2 Methods

This section introduces measure transport using KSD. In Section 2.1 and Section 2.2 we recall mathematical definitions from measure transport and Hilbert spaces, respectively; in Section 2.3 we recall the definition and properties of KSD; in Section 2.4 we formally define our proposed method, and in Section 2.5 we present some parametric families  $\mathcal{T}$  that can be employed.

**Notation:** The set of probability measures on a measurable space  $\mathcal{X}$  is denoted  $\mathcal{P}(\mathcal{X})$  and a point mass at  $x \in \mathcal{X}$  is denoted  $\delta(x) \in \mathcal{P}(\mathcal{X})$ . For  $P \in \mathcal{P}(\mathcal{X})$  let  $L^q(P) := \{f : \mathcal{X} \rightarrow \mathbb{R} : \int f^q dP < \infty\}$ . For  $P \in \mathcal{P}(\mathbb{R}^d)$  and  $(P_n)_{n \in \mathbb{N}} \subset \mathcal{P}(\mathbb{R}^d)$ , let  $P_n \Rightarrow P$  denote weak convergence of the sequence of measures  $(P_n)_{n \in \mathbb{N}}$  to  $P$ . The Euclidean norm on  $\mathbb{R}^n$  is denoted  $\|\cdot\|$ . Partial derivatives are denoted  $\partial_x$ . For a function  $f : \mathbb{R}^n \rightarrow \mathbb{R}$  the gradient is defined as  $[\nabla f]_i = \partial_{x_i} f$ . For a function  $f = (f_1, \dots, f_m) : \mathbb{R}^n \rightarrow \mathbb{R}^m$ , the divergence is defined as  $\nabla \cdot f = \sum_{i=1}^n \partial_{x_i} f_i$ .

Our main results in this paper concern the Euclidean space  $\mathbb{R}^d$ , but in some parts of the paper, such as Section 2.1, it is possible to state definitions at a greater level of generality at no additional effort - in such situations we do so.

## 2.1 Measure Transport

A *Borel space*  $\mathcal{X}$  is a topological space equipped with its Borel  $\sigma$ -algebra, denoted  $\Sigma_{\mathcal{X}}$ . Throughout this paper we restrict attention to Borel spaces  $\mathcal{X}$  and  $\mathcal{Y}$ . Let  $Q \in \mathcal{P}(\mathcal{X})$  and  $P \in \mathcal{P}(\mathcal{Y})$ . In the parlance of measure transport,  $Q$  is the *reference* and  $P$  the *target*. Let  $T : \mathcal{X} \rightarrow \mathcal{Y}$  be a measurable function and define the *pushforward* of  $Q$  through  $T$  as the probability measure  $T_{\#}Q \in \mathcal{P}(\mathcal{Y})$  that assigns mass  $(T_{\#}Q)(A) = Q(T^{-1}(A))$  to each  $A \in \Sigma_{\mathcal{Y}}$ . Here  $T^{-1}(A) = \{x \in \mathcal{X} : T(x) \in A\}$  denotes the pre-image of  $A$  under  $T$ . Such a function  $T$  is called a *transport map* from  $Q$  to  $P$  if  $T_{\#}Q = P$ .

Faced with a complicated distribution  $P$ , if one can express  $P$  using a transport map  $T$  and a distribution  $Q$  that can be sampled, then samples from  $P$  can be generated by applying  $T$  to samples from  $Q$ . This idea underpins elementary methods for numerical simulation of random variables [Devroye, 2013]. However, in posterior approximation it will not typically be straightforward to identify a transport map and at best one can seek an *approximate* transport map, for which  $T_{\#}Q$  approximates  $P$  in some sense to be specified. In this paper we seek approximations in the sense of KSD, which is formally introduced in Section 2.3 and requires concepts in Section 2.2, next.

## 2.2 Hilbert Spaces

A Hilbert space  $\mathcal{H}$  is a complete inner product space; in this paper we use subscripts, such as  $\langle \cdot, \cdot \rangle_{\mathcal{H}}$ , to denote the associated inner product. Given two Hilbert spaces  $\mathcal{G}$ ,  $\mathcal{H}$ , the *Cartesian product*  $\mathcal{G} \times \mathcal{H}$  is again a Hilbert space equipped with the inner product  $\langle (g_1, h_1), (g_2, h_2) \rangle_{\mathcal{G} \times \mathcal{H}} := \langle g_1, g_2 \rangle_{\mathcal{G}} + \langle h_1, h_2 \rangle_{\mathcal{H}}$ . In what follows we let  $\mathcal{B}(\mathcal{H}) := \{h \in \mathcal{H} : \langle h, h \rangle_{\mathcal{H}} \leq 1\}$  denote the unit ball in a Hilbert space  $\mathcal{H}$ .

From the Moore–Aronszajn theorem [Aronszajn, 1950], any symmetric positive definite function  $k : \mathcal{Y} \times \mathcal{Y} \rightarrow \mathbb{R}$  defines a unique *reproducing kernel Hilbert space* of real-valued functions on  $\mathcal{Y}$ , denoted  $\mathcal{H}_k$  and with inner-product denoted  $\langle \cdot, \cdot \rangle_{\mathcal{H}_k}$ . Indeed,  $\mathcal{H}_k$  is a Hilbert space characterised by the properties (i)  $k(\cdot, y) \in \mathcal{H}_k$  for all  $y \in \mathcal{Y}$ , (ii)  $\langle h, k(\cdot, y) \rangle_{\mathcal{H}_k} = h(y)$  for all  $h \in \mathcal{H}_k$ ,  $y \in \mathcal{Y}$ . Reproducing kernels are central to KSD, as described next.

## 2.3 Kernel Stein Discrepancy

Stein discrepancies were introduced in Gorham and Mackey [2015] to provide a notion of discrepancy that is computable in the Bayesian statistical context. In this paper we focus on so-called *kernel Stein discrepancy* [KSD; Liu et al., 2016, Chwialkowski et al., 2016, Gorham and Mackey, 2017] since this has lower computational overhead compared to the original proposal of Gorham and Mackey [2015].

The construction of KSD relies on Stein’s method [Stein, 1972] where, for a possibly complicated probability measure  $P \in \mathcal{P}(\mathcal{Y})$  of interest, one identifies a *Stein set*  $\mathcal{F}$  and a *Stein operator*  $\mathcal{A}_P$ , such that  $\mathcal{A}_P$  acts on elements  $f \in \mathcal{F}$  to return functions  $\mathcal{A}_P f : \mathcal{Y} \rightarrow \mathbb{R}$  with the property that

$$P' = P \quad \text{iff} \quad \mathbb{E}_{Y \sim P'}[(\mathcal{A}_P f)(Y)] = 0 \quad \forall f \in \mathcal{F} \quad (2)$$

for all  $P' \in \mathcal{P}(\mathcal{Y})$ . A *Stein discrepancy* uses the extent to which (2) is violated to quantify the discrepancy between  $P'$  and  $P$ :

$$\mathcal{D}_S(P, P') := \sup_{f \in \mathcal{F}} |\mathbb{E}_{Y \sim P'}[(\mathcal{A}_P f)(Y)]|$$

Note that  $\mathcal{D}_S$  is not symmetric in its arguments. For  $\mathcal{Y} = \mathbb{R}^d$  and suitably regular  $P$ , which admits a positive and differentiable density function  $p$ , Liu et al. [2016], Chwialkowski et al. [2016] showed that one may take  $\mathcal{F}$  to be a set of smooth vector fields  $f : \mathbb{R}^d \rightarrow \mathbb{R}^d$  and  $\mathcal{A}_P$  to be a carefully chosen differential operator on  $\mathbb{R}^d$ . More precisely, and letting  $s_p := \nabla \log p$ , we have Theorem 1 below, which is due to Gorham and Mackey [2017, Theorem 7]:

**Definition 1** (Eberle [2015]). *A probability measure  $P \in \mathcal{P}(\mathbb{R}^d)$  is called distantly dissipative if  $\liminf_{r \rightarrow \infty} \kappa(r) > 0$ , where*

$$\kappa(r) := -r^{-2} \inf_{\|x-y\|=r} \langle s_p(x) - s_p(y), x - y \rangle.$$

**Theorem 1.** *Suppose that  $P \in \mathcal{P}(\mathbb{R}^d)$  is distantly dissipative. For some  $c > 0$ ,  $\ell > 0$  and  $\beta \in (-1, 0)$ , let*

$$\mathcal{F} := \mathcal{B}\left(\prod_{i=1}^d \mathcal{H}_k\right), \quad k(x, y) := (c^2 + \|\frac{x-y}{\ell}\|^2)^\beta \quad (3)$$

$$\mathcal{A}_P f := f \cdot \nabla \log p + \nabla \cdot f. \quad (4)$$

*Then (2) holds. Moreover, if  $\mathcal{D}_S(P, P_n) \rightarrow 0$ , then  $P_n \Rightarrow P$ .*

The kernel  $k$  appearing in (3) is called the *inverse multi-quadric* kernel. It is known that the elements of  $\mathcal{H}_k$  are smooth functions, which justifies the application of the differential operator. The last part of Theorem 1 clarifies why KSD is useful; convergence in KSD controls the standard notion of weak convergence of measures to  $P$ .

KSD, in contrast to KLD, is well-defined when the approximating measure  $P'$  and the target  $P$  differ in their support. Moreover, in some situations KSD can be exactly computed: from Liu et al. [2016, Theorem 3.6] or equivalently Chwialkowski et al. [2016, Theorem 2.1],

$$\mathcal{D}_S(P, P') = \sqrt{\mathbb{E}_{Y, Y' \sim P'}[u_p(Y, Y')]} \quad (5)$$

$$u_p(y, y') := s_p(y)^\top k(y, y') s_p(y') + s_p(y)^\top \nabla_{y'} k(y, y') + \nabla_y k(y, y')^\top s_p(y') + \nabla_y \cdot \nabla_{y'} k(y, y'). \quad (6)$$

It follows that KSD can be exactly computed whenever  $P'$  has a finite support and  $s_p$  can be evaluated on this support:

$$\mathcal{D}_S(P, \frac{1}{n} \sum_{i=1}^n \delta(y_i)) = \sqrt{\frac{1}{n^2} \sum_{i,j=1}^n u_p(y_i, y_j)}. \quad (7)$$

Computation of (7) can proceed with  $p$  available up to an unknown normalisation constant, facilitating application in the Bayesian context. Now we are in a position to present our proposed method.

## 2.4 Measure Transport with KSD

Our proposed method for posterior approximation is simply stated at a high level; we attempt to solve (1) with  $\mathcal{D} = \mathcal{D}_S$  and over a set  $\mathcal{T}$  of candidate functions  $T^\theta : \mathcal{X} \rightarrow \mathcal{Y}$  indexed by a finite-dimensional parameter  $\theta \in \Theta$ . That is, we aim to solve

$$\arg \min_{\theta \in \Theta} \mathcal{D}_S(P, T_\#^\theta Q). \quad (8)$$

Discussion of the choice of  $\mathcal{T}$  is deferred until Section 2.5. Compared to previous approaches to measure transport using KLD [Rezende and Mohamed, 2015, Kingma et al., 2016, Marzouk et al., 2016, Parno and Marzouk, 2018], KSD is arguably more computationally and theoretically tractable; the computational aspects will now be described.

The solution of (8) is equivalent to minimisation of the function  $F(\theta) := \mathcal{D}_S(P, T_\#^\theta Q)^2$  over  $\theta \in \Theta$ . In order to employ state-of-the-art algorithms for stochastic optimisation, an unbiased estimator for the gradient  $\nabla_\theta F(\theta)$  is required. A naive starting point would be to differentiate the expression for the KSD of an empirical measure in (7), however the resulting *V-statistic* is biased. Under weak conditions, we establish instead the following unbiased estimator (a *U-statistic*) for the gradient:

**Proposition 1.** *Let  $\Theta \subseteq \mathbb{R}^p$  be an open set. Assume that  $\forall \theta \in \Theta$*

(A1)  *$(x, x') \mapsto u_p(T^\theta(x), T^\theta(x'))$  is measurable;*

(A2)  *$\mathbb{E}_{X, X' \sim Q} [|u_p(T^\theta(X), T^\theta(X'))|] < \infty$ ;*

(A3)  *$\mathbb{E}_{X, X' \sim Q} [\|\nabla_\theta u_p(T^\theta(X), T^\theta(X'))\|] < \infty$ ;*

*and that  $\forall x, x' \in \mathcal{X}$ ,*

(A4)  *$\theta \mapsto \nabla_\theta u_p(T^\theta(x), T^\theta(x'))$  is continuous.*

*Then  $\forall \theta \in \Theta$*

$$\nabla_\theta F(\theta) = \mathbb{E} \left[ \frac{1}{n(n-1)} \sum_{i \neq j} \nabla_\theta u_p(T^\theta(x_i), T^\theta(x_j)) \right],$$

*where the expectation is taken with respect to independent samples  $x_1, \dots, x_n \sim Q$ .*

All proofs are contained in Appendix A. The assumptions on  $u_p$  amount to assumptions on  $T$ ,  $p$  and  $k$ , by virtue of (6). It is not difficult to find explicit assumptions on  $T$ ,  $p$  and  $k$  that imply (A1-4), but these may be stronger than required and we prefer to present the most general result.

Armed with an unbiased estimator of the gradient, we can employ a stochastic optimisation approach, such as stochastic gradient descent [SGD; Robbins and Monro, 1951] or adaptive moment estimation [Adam; Kingma and Ba, 2015]. See Kushner and Yin [2003], Ruder [2016]. For the results reported in the main text we used Adam, with  $\theta$  initialised as described in Appendix C.1, but other choices were investigated (see Appendix C.2).

## 2.5 Parametric Transport Maps

In this section we describe some existing classes of transport map  $T : \mathcal{X} \rightarrow \mathcal{Y}$  that are compatible with KSD measure transport. From Proposition 1 we see that measure transport using KSD does not impose strong assumptions on the transport map. Indeed, compared to KLD [Rezende and Mohamed, 2015, Kingma et al., 2016, Marzouk et al., 2016, Parno and Marzouk, 2018] we do not require that  $T$  is a diffeomorphism ( $T$  need not even be continuous, nor a bijection), making our framework considerably more general. This additional flexibility may allow measure to be transported more efficiently, using simpler maps. That being said, if one wishes to compute the density of  $T_{\#}Q$  (in addition to sampling from  $T_{\#}Q$ ), then a diffeomorphism, along with the usual change-of-variables formula, should be used.

**Triangular Maps:** Rosenblatt [1952] and Knothe et al. [1957] observed that, for  $P, Q \in \mathcal{P}(\mathbb{R}^d)$  admitting densities, a transport map  $T : \mathbb{R}^d \rightarrow \mathbb{R}^d$  can without loss of generality be sought in the *triangular form*

$$T(x) = (T_1(x_1), T_2(x_1, x_2), \dots, T_d(x_1, \dots, x_d)), \quad (9)$$

where each  $T_i : \mathbb{R}^i \rightarrow \mathbb{R}$  and  $x = (x_1, \dots, x_d)$  [Bogachev et al., 2005, Lemma 2.1]. The triangular form was used in Marzouk et al. [2016], Parno and Marzouk [2018], since the Jacobian determinant, that is required when using KLD (but not KSD), can exploit the fact that  $\nabla T$  is triangular to maintain linear complexity in  $d$ .

**Maps from Measure Transport:** In the context of a triangular map  $T = (T_1, \dots, T_d)$ , Marzouk et al. [2016] and Parno and Marzouk [2018] considered several parametric models for the components  $T_i$ , including polynomials, radial basis functions and monotone parameterisations of the form

$$T_i(x_1, \dots, x_i) = f_i(x_1, \dots, x_{i-1}) + \int_0^{x_i} \exp(g_i(x_1, \dots, x_{i-1}, y)) dy,$$

for functions  $f_i : \mathbb{R}^{i-1} \rightarrow \mathbb{R}$  and  $g_i : \mathbb{R}^i \rightarrow \mathbb{R}$ . The monotone parameterisation ensures that  $\det \nabla T > 0$  on  $\mathbb{R}^d$ , which facilitates computation of the density of  $T_{\#}P$ , as required for

KLD<sup>2</sup>.

**Maps from Normalising Flows:** The principal application of normalising flows is density estimation [Papamakarios et al., 2019, Kobyzev et al., 2020], but the parametric families of transport map used in this literature can also be used for posterior approximation [Rezende and Mohamed, 2015].

A normalising flow is required to be a diffeomorphism  $T : \mathbb{R}^d \rightarrow \mathbb{R}^d$  with the property that the density of  $T_{\#}Q$  can be computed.

A popular choice that exploits the triangular form (9) is an *autoregressive flow*  $T_i(x) = \tau(c_i(x_1, \dots, x_{i-1}), x_i)$ , where  $\tau$  is a monotonic transformation of  $x_i$  parameterised by  $c_i$ , e.g. an affine transformation  $T_i(x) = \alpha_i x_i + \beta_i$  where  $c_i$  outputs  $\alpha_i \neq 0$  and  $\beta_i$ . For instance, Kingma et al. [2016] proposed *inverse autoregressive flows* (IAF), taking  $T(x) = \mu + \exp(\sigma) \odot x$ . Here  $\odot$  is elementwise multiplication and  $\mu$  and  $\sigma$  are vectors output by an autoregressive neural network: one designed so that  $\mu_i, \sigma_i$  depend on  $x$  only through  $x_j$  for  $j < i$ . In Huang et al. [2018],  $\tau$  was the output of a monotonic neural network and the resulting flow was called a *neural autoregressive flow* (NAF).

Compositions of normalising flows can also be considered, of the form

$$T = T^{(n)} \circ \dots \circ T^{(1)} \quad (10)$$

where each  $T^{(i)}$  is itself a normalising flow e.g. a IAF. For instance, Dinh et al. [2014] proposed using *coupling layers* of the form  $T^{(i)}(x) = (h(x_1, \dots, x_r), x_{r+1}, \dots, x_d)$ , where  $r < d$  and  $h : \mathbb{R}^r \rightarrow \mathbb{R}^r$  is a bijection. These only update the first  $r$  components of  $x$ , so they are typically composed with permutations.

Regardless of the provenance of a transport map  $T$ , all free parameters of  $T$  are collectively denoted  $\theta$ , and are to be estimated. The suitability of a parametric set of candidate maps in combination with KSD is studied both empirically in Section 4 and theoretically, next.

### 3 Theoretical Assessment

In Section 3.1 we affirm basic conditions on  $P$  and  $Q$  for a transport map to exist. In Section 3.2 we establish sufficient conditions for the consistency of our method and in Section 3.3 we consider a particular class of transport maps based on neural networks, to demonstrate how our conditions on the transport map can be explicitly validated.

---

<sup>2</sup>For polynomials and radial basis functions, these authors only enforced  $\det \nabla T > 0$  locally, introducing an additional approximation error in evaluation of KLD; such issues do not arise with KSD.



### 3.1 Existence of an $L^2$ Transport Map

For a complete separable metric space  $\mathcal{X}$ , recall that the *Wasserstein space* of order  $p \geq 1$  is defined by taking some  $x_0 \in \mathcal{X}$  and

$$\mathcal{P}_p(\mathcal{X}) := \{P \in \mathcal{P}(\mathcal{X}) : \int \text{dist}(x, x_0)^p dP(x) < \infty\},$$

where the definition is in fact independent of the choice of  $x_0 \in \mathcal{X}$  [Villani, 2009, Definition 6.4]. For existence of a transport map, we make the following assumptions on  $P$  and  $Q$ :

**Assumption 1** (Assumptions on  $Q$ ). *The reference measure  $Q \in \mathcal{P}(\mathcal{X})$ , where  $\mathcal{X}$  is a complete separable metric space, and  $Q(\{x\}) = 0$  for all  $x \in \mathcal{X}$ .*

**Assumption 2** (Assumptions on  $P$ ). *The target measure  $P \in \mathcal{P}_2(\mathbb{R}^d)$  has a strictly positive density  $p$  on  $\mathbb{R}^d$ .*

These assumptions guarantee the existence of a transport map with  $L^2$  regularity, as shown in the following result:

**Proposition 2.** *If Assumptions 1 and 2 hold, then there exists a transport map  $T \in \prod_{i=1}^d L^2(Q)$  such that  $T_{\#}Q = P$ .*

Of course, such a transport map will not be unique in general.

### 3.2 Consistent Posterior Approximation

The setting for our theoretical analysis considers a sequence  $(\mathcal{T}_n)_{n \in \mathbb{N}}$  of parametric classes of transport map, where intuitively  $\mathcal{T}_n$  provides a more flexible class of map as  $n$  is increased. For example,  $\mathcal{T}_n$  could represent the class of triangular maps comprising of  $n$ th order polynomials, or a class of normalising flows comprising of  $n$  layers in (10).

**Assumption 3** (Assumptions on  $\mathcal{T}_n$ ). *There exists a subset  $\mathfrak{T} \subseteq \prod_{i=1}^d L^2(Q)$  containing an element  $T \in \mathfrak{T}$  for which  $T_{\#}Q = P$ . The sequence  $(\mathcal{T}_n)_{n \in \mathbb{N}}$  satisfies  $\mathcal{T}_n \subseteq \mathfrak{T}$  with  $\mathcal{T}_n \subseteq \mathcal{T}_m$  for  $n \leq m$  and  $\mathcal{T}_{\infty} := \lim_{n \rightarrow \infty} \mathcal{T}_n$  is a dense set in  $\mathfrak{T}$ .*

Proposition 2 provides sufficient conditions for the set  $\mathfrak{T}$  in Assumption 3 to exist; the additional content of Assumption 3 ensures that  $\mathcal{T}_{\infty}$  is rich enough to consistently approximate an exact transport map, in principle at least. Next, we state our consistency result:

**Theorem 2.** *Let Assumptions 1 to 3 hold. Further suppose that  $P$  is distantly dissipative, with  $\nabla \log p$  Lipschitz and  $\mathbb{E}_{X \sim P}[\|\nabla \log p(X)\|^2] < \infty$ . Suppose that  $T_n \in \mathcal{T}_n$  satisfies*

$$\mathcal{D}_S(P, (T_n)_{\#}Q) - \inf_{T \in \mathcal{T}_n} \mathcal{D}_S(P, T_{\#}Q) \xrightarrow{n \rightarrow \infty} 0, \quad (11)$$

*with  $\mathcal{D}_S$  defined in Theorem 1. Then  $(T_n)_{\#}Q \Rightarrow P$ .*

The statement in (11) accommodates the reality that, although finding the global optimum  $T \in \mathcal{T}_n$  will typically be impractical, one can realistically expect to find an element  $T_n$  that achieves an almost-as-low value of KSD, e.g. using a stochastic optimisation method. To our knowledge, no comparable consistency guarantees exist for measure transport using KLD.

### 3.3 Validating our Assumptions on $\mathcal{T}_n$

Recall that earlier work on measure transport placed strong restrictions on the set of maps  $\mathcal{T}_n$ , requiring each map to be a diffeomorphism with non-vanishing Jacobian determinant. In contrast, our assumptions on  $\mathcal{T}_n$  are almost trivial; we do not require smoothness and there is not a bijection requirement. Our assumptions can be satisfied *in principle* whenever  $\mathcal{X}$  is a complete separable metric space, since then  $\prod_{i=1}^d L^2(Q)$  is separable [Cohn, 2013, Proposition 3.4.5] and admits a Schauder basis  $\{\phi_i\}_{i \in \mathbb{N}}$ , so we may take  $\mathcal{T}_n = \text{span}\{\phi_1, \dots, \phi_n\}$  for Assumption 3 to hold. In practice we are able to verify Assumption 3 for quite non-trivial classes of map  $\mathcal{T}_n$ . To demonstrate, one such example is presented next:

We consider deep neural networks with multi-layer perceptron architecture and ReLU activation functions. Let  $\mathcal{R}_{l,n}(\mathbb{R}^p \rightarrow \mathbb{R}^d)$  denote the set of such *ReLU neural networks*  $f : \mathbb{R}^p \rightarrow \mathbb{R}^d$  with  $l$  layers and width at most  $n$ . See Definition 4 in Appendix A.4 for a formal definition.

**Proposition 3.** *Let Assumptions 1 and 2 hold. Let  $Q$  admit a positive, continuous and bounded density on  $\mathcal{X} = \mathbb{R}^p$ . Let  $\mathcal{T}_n = \mathcal{R}_{l,n}(\mathbb{R}^p \rightarrow \mathbb{R}^d)$  with  $l := \lceil \log_2(p+1) \rceil$ . Then Assumption 3 holds.*

The maps in Proposition 3 are not bijections, illustrating the greater flexibility of KSD compared to KLD for measure transport. This completes our theoretical discussion, and our attention now turns to empirical assessment.

## 4 Empirical Assessment

The purpose of this section is to investigate whether KSD is competitive with KLD for measure transport. Section 4.1 compares both approaches using a variety of transport maps and a synthetic test-bed. Then, in Sections 4.2 and 4.3 we consider more realistic posterior approximation problems arising from, respectively, a biochemical oxygen model and a parametric differential equation model.

In all experiments we used the kernel (3) with  $c = 1$ ,  $\ell = 0.1$ ,  $\beta = -1/2$  (other choices were investigated in Appendix C.5), the stochastic optimiser Adam with batch size  $n = 100$  and learning rate 0.001 (other choices were investigated in Appendix C.2), and the reference distribution  $Q$  was taken to be a standard Gaussian on  $\mathbb{R}^p$  (other choices were considered in Appendix C.4). Code to reproduce these results is available at <https://github.com/MatthewAlexanderFisher/MTKSD>.

### 4.1 Synthetic Test-Bed

First we consider a set of synthetic examples that have previously been used to motivate measure transport as an alternative to MCMC. Three targets were considered;  $p_1$  is a sinusoidal density,  $p_2$  is a banana density and  $p_3$  is multimodal; these are formally defined in Appendix B.2. Results for  $p_1$  and  $p_3$  are displayed in Figure 1. The convergence of the

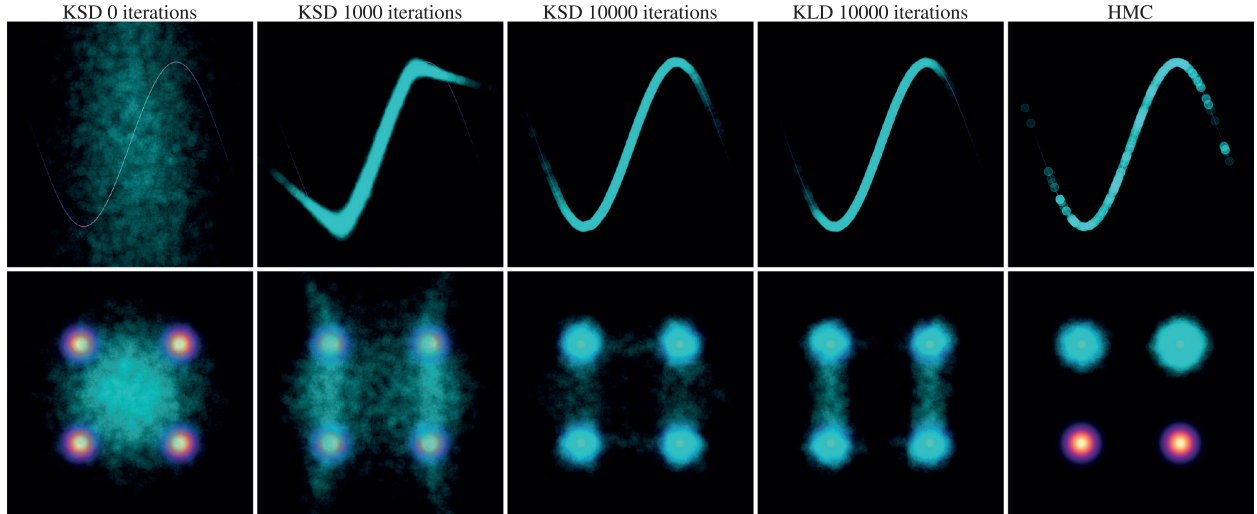


Figure 1: Measure transport with KSD, versus KLD and HMC. The top row reports results for approximation of a sinusoidal density using an inverse autoregressive flow, while the bottom row reports analogous results for a multimodal density and a neural autoregressive flow. The first three columns display convergence of the KSD-based method as the number of iterations of stochastic optimisation is increased. The remaining columns compare the output of the KLD-based method and HMC for an identical computational budget.

approximation to the target is shown for KSD and the corresponding approximation after  $10^4$  iterations of Adam is shown for KLD. Since, for both objectives, one iteration requires  $10^2$  evaluations of  $\log p_i$  or its gradient, this represents a total of  $10^6$  calls to  $\log p_i$  or its gradient. The corresponding approximation produced using an adaptive Hamiltonian Monte Carlo (HMC) algorithm [Hoffman and Gelman, 2014, Betancourt, 2017] is shown, where the HMC chains were terminated once  $10^6$  evaluations of  $\log p_i$  or its gradient had been performed. Both  $p_1$  and  $p_3$  present challenges for HMC that, to some extent, can be overcome using measure transport.

The results in Figure 1 are for a fixed class of transport map, but now we report a systematic comparison of KSD and KLD. The majority of maps that we consider are diffeomorphic (in order that KLD can be used), implemented in Pyro [Bingham et al., 2018]. Since KSD does not place such requirements on the transport map, we also report results for a (non-bijective) ReLU neural network. Our performance measure is an estimate of the Wasserstein-1 distance between the target and approximate distributions computed using  $10^4$  samples (see Appendix B.1 for details). Results are detailed in Table 1.

Overall, there is no clear sense in which KSD out-performs KLD or *vice versa*; KSD performed best on  $p_1$ , KLD performed best on  $p_2$ , and for  $p_3$  the results were mixed. We conclude that these objectives offer similar performance for measure transport. However, KLD cannot be applied to the ReLU neural network (denoted N/A in Table 1) due to the strong constraints on the mapping that are required by KLD.

Two discussion points are now highlighted: First, it is known that certain normalising

Transport Map	$N$	Sinusoidal		Banana		Multimodal	
		KSD	KLD	KSD	KLD	KSD	KLD
IAF	$10^4$	<b>0.38</b>	0.52	0.20	<b>0.07</b>	<b>0.67</b>	1.1
IAF (stable)	$10^4$	<b>0.35</b>	0.39	0.16	<b>0.11</b>	<b>0.61</b>	0.62
NAF	$10^4$	<b>0.55</b>	0.64	0.39	<b>0.025</b>	<b>0.095</b>	0.11
SAF	$10^4$	<b>0.23</b>	0.58	0.20	<b>0.18</b>	<b>0.30</b>	0.48
B-NAF	$10^4$	<b>0.78</b>	1.2	0.70	<b>0.18</b>	1.0	<b>0.99</b>
Polynomial (cubic)	$10^4$	<b>0.40</b>	0.84	0.25	<b>0.059</b>	0.51	<b>0.43</b>
IAF mixture	$3 \times 10^4$	1.29	<b>0.61</b>	0.19	<b>0.14</b>	0.037	<b>0.036</b>
ReLU network	$5 \times 10^4$	<b>0.71</b>	N/A	<b>0.43</b>	N/A	<b>0.22</b>	N/A

Table 1: Results from the synthetic test-bed. The first column indicates which parametric class of transport map was used; full details for each class can be found in Appendix B.2. A map-dependent number of iterations of stochastic optimisation,  $N$ , are reported - this is to ensure that all optimisers approximately converged. The main table reports the (first) Wasserstein distance between the approximation  $T_{\#}Q$  and the target  $P$ . Bold values indicate which of KSD or KLD performed best.

flows can capture multiple modes due to their flexibility, however others cannot [Huang et al., 2018]. One solution is to consider a mixture of transport maps; i.e.  $\sum_{i=1}^d w_i T_{\#}^{(i)} Q_i$  with reference distribution  $Q_1 \times \dots \times Q_d$  and mixing weights  $w_i > 0$  satisfying  $\sum_i w_i = 1$ . This idea has been explored recently in Pires and Figueiredo [2020]. In Table 1 we report results using mixtures of *inverse autoregressive flows* (IAF). As one might hope, these approximations were successful in finding each of the modes in  $p_3$ , but fared relatively worse for  $p_1$  and  $p_2$ . Second, since in Adam we are using a Monte Carlo estimator of the gradient, it is natural to ask whether a quasi Monte Carlo estimator would offer an improvement [Wenzel et al., 2018]. This was investigated and our results are reported in Appendix C.3.

## 4.2 Biochemical Oxygen Demand Model

Next we reproduce an experiment that was used to illustrate measure transport using KLD in Parno and Marzouk [2018]. The task is parameter inference in a  $d = 2$  dimensional oxygen demand model, of the form  $B(t) = \alpha_1(1 - \exp(-\alpha_2 t))$ , where  $B(t)$  is the biochemical oxygen demand at time  $t$ , a measure of the consumption of oxygen in a given water column sample due to the decay of organic matter [Sullivan et al., 2010]. The parameters to be inferred are  $\alpha_1, \alpha_2 > 0$ .

Full details of the prior and the likelihood are contained in Appendix B.3.

For our experiment, we trained a *block neural autoregressive flow*<sup>3</sup> using  $N = 30,000$  iterations of Adam. Results are presented in Figure 2. Unlike the synthetic experiments, we no longer have a closed form for the target  $P$ ; however, this problem was amenable to MCMC

<sup>3</sup>This class of transport map was experimentally observed to outperform the other classes we considered.

and a long run of HMC ( $10^6$  iterations, thinned by a factor of 100) provided a gold standard, allowing us to approximate the Wasserstein-1 distance from  $T_{\#}Q$  to  $P$  as in Section 4.1. For the KSD-based method, we obtained a Wasserstein-1 distance of 0.069, while KLD achieved 0.015.

Although the Wasserstein-1 distance for KSD is larger than that for KLD, both values are close to the *noise floor* for our approximation of the Wasserstein-1 distance; two independent runs of HMC ( $10^6$  iterations, thinned by a factor of 100), differed in Wasserstein-1 distance by 0.022. We therefore conclude that KSD and KLD performed comparably on this task.

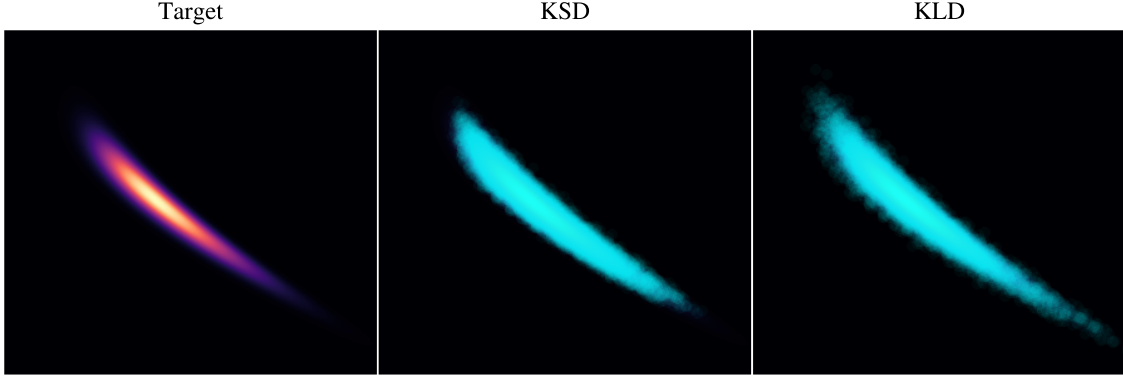


Figure 2: Results for the biochemical oxygen demand model. The leftmost panel is the target distribution, while the central and rightmost panels show samples generated from the output of the methods based, respectively, on KSD and KLD.

### 4.3 Generalised Lotka-Volterra Model

Our final experiment is a realistic inference problems involving a non-trivial likelihood. Following Parno and Marzouk [2018], we consider parameter inference for a generalised Lotka–Volterra model

$$\begin{aligned}\frac{dp}{dt}(t) &= rp(t)\left(1 - \frac{p(t)}{k}\right) - s\frac{p(t)q(t)}{a+p(t)}, \\ \frac{dq}{dt}(t) &= u\frac{p(t)q(t)}{a+p(t)} - vq(t),\end{aligned}\tag{12}$$

where  $p(t), q(t) > 0$  are the predator and prey populations respectively at time  $t$  and  $r, k, s, u, a$  and  $v$ , along with the initial conditions  $p(0) = p_0$  and  $q(0) = q_0$ , are parameters to be inferred. Together, these  $d = 8$  parameters were inferred from a noisy dataset, with the prior and likelihood reported in Appendix B.4. This task is realistic and yet amenable to MCMC; the latter is an essential requirement to allow us to provide a gold standard against which to assess KSD and KLD, and we again used an extended run of HMC.

For this experiment, the B-NAF class and  $N = 5 \cdot 10^4$  iterations of Adam were used. The gradients, required both for HMC and KSD measure transport, were computed using automatic differentiation through the numerical integrator used to solve (12), implemented in the `torchdiffeq` Python package [Chen et al., 2018].

For the KSD-based method, we obtained an approximate Wasserstein-1 distance from  $T_{\#}Q$  to  $P$  of 0.130, while KLD achieved 0.110. The noise floor for our approximation of the Wasserstein-1 distance in this case was 0.107. We therefore conclude that KSD and KLD also performed comparably on this more challenging task.

## 5 Discussion

This paper proposed and studied measure transport using KSD, which can be seen as an instance of *operator variational inference* [Ranganath et al., 2016]. Our findings suggest that KSD is a suitable variational objective for measure transport; we observed empirical performance comparable with that of KLD, yet only minimal and verifiable conditions on the map  $T$  were required.

There are three potential limitations of KSD compared to KLD: First, the parameters of the kernel must be specified, and a poor choice of kernel parameters can result in poor approximation; see Appendix C.5.

It would be interesting to explore whether adversarial maximisation of KSD with respect to the kernel parameters, while minimising KSD over the choice of transport map, offers a solution [Grathwohl et al., 2020]. Second, while only first order derivatives are required for KLD, gradient-based optimisation of KSD requires second order derivatives of  $p$ . In most automatic differentiation frameworks, and for most models, this is possible at little extra computational cost, but sometimes this will present difficulties e.g. for models with differential equations involved. Third, it is known that score-based variational objectives can sometimes exhibit pathologies [Wenliang, 2020]; some of these are illustrated in Appendix C.8.

Several recent works explored the possibility of combining measure transport with Monte Carlo [Salimans et al., 2015, Wolf et al., 2016, Hoffman, 2017, Caterini et al., 2018, Prangle, 2019, Thin et al., 2020] and it would also be interesting to consider the use of KSD in that context. Related, for both KSD and KLD there is freedom to select the space  $\mathcal{X}$  and the reference distribution  $Q$ . This could also be handled within the optimisation framework, but further work would be needed to determine how these additional degrees of freedom should be parametrised.

**Acknowledgements:** MAF was supported by the EPSRC Centre for Doctoral Training in Cloud Computing for Big Data EP/L015358/1 at Newcastle University, UK. THN was supported by a Fulbright scholarship, an American Australian Association scholarship and a Roberta Sykes scholarship. MMG and CJO were supported by the Lloyd’s Register Foundation programme on data-centric engineering at the Alan Turing Institute, UK. The authors thank Onur Teymur for helpful comments on the manuscript.

## References

- Charalambos D Aliprantis and Owen Burkinshaw. *Principles of Real Analysis*. Academic Press, 1998.
- Martin Arjovsky, Soumith Chintala, and Léon Bottou. Wasserstein generative adversarial networks. In *Proceedings of the 34th International Conference on Machine Learning-Volume 70*, pages 214–223, 2017.
- Nachman Aronszajn. Theory of reproducing kernels. *Transactions of the American Mathematical Society*, 68(3):337–404, 1950.
- Raman Arora, Amitabh Basu, Poorya Mianjy, and Anirbit Mukherjee. Understanding deep neural networks with rectified linear units. In *Proceedings of the 6th International Conference on Learning Representations*, 2018.
- Khai Xiang Au, Matthew M Graham, and Alexandre H Thiery. Manifold lifting: Scaling MCMC to the vanishing noise regime. *arXiv:2003.03950*, 2020.
- Michael Betancourt. A conceptual introduction to Hamiltonian Monte Carlo. *arXiv:1701.02434*, 2017.
- MJ Betancourt, Simon Byrne, and Mark Girolami. Optimizing the integrator step size for Hamiltonian Monte Carlo. *arXiv:1411.6669*, 2014.
- Patrick Billingsley. *Probability and Measure*. John Wiley and Sons, 1979.
- Eli Bingham, Jonathan P. Chen, Martin Jankowiak, Fritz Obermeyer, Neeraj Pradhan, Theofanis Karaletsos, Rohit Singh, Paul Szerlip, Paul Horsfall, and Noah D. Goodman. Pyro: Deep universal probabilistic programming. *Journal of Machine Learning Research*, 20(18):403, 2018.
- David M. Blei, Alp Kucukelbir, and Jon D. McAuliffe. Variational inference: A review for statisticians. *Journal of the American Statistical Association*, 112(518):859–877, 2017.
- V I Bogachev, A V Kolesnikov, and K V Medvedev. Triangular transformations of measures. *Sbornik: Mathematics*, 196(3):309–335, apr 2005. doi: 10.1070/sm2005v196n03abeh000882. URL <https://doi.org/10.1070%2Fsm2005v196n03abeh000882>.
- KC Border. Differentiating an integral: Leibniz’ rule. Technical report, Caltech Division of the Humanities and Social Sciences, 2016.
- Johann Brehmer and Kyle Cranmer. Flows for simultaneous manifold learning and density estimation. *arXiv:2003.13913*, 2020.

- Alexander Buchholz, Florian Wenzel, and Stephan Mandt. Quasi-Monte Carlo variational inference, 2018.
- Nicola De Cao, Ivan Titov, and Wilker Aziz. Block neural autoregressive flow. In *Proceedings of the 35th Conference on Uncertainty in Artificial Intelligence*, 2019.
- Bob Carpenter, Andrew Gelman, Matthew D Hoffman, Daniel Lee, Ben Goodrich, Michael Betancourt, Marcus Brubaker, Jiqiang Guo, Peter Li, and Allen Riddell. Stan: A probabilistic programming language. *Journal of Statistical Software*, 76(1), 2017.
- Anthony L Caterini, Arnaud Doucet, and Dino Sejdinovic. Hamiltonian variational auto-encoder. In *Proceedings of the 32nd Conference on Neural Information Processing Systems*, pages 8167–8177, 2018.
- Ricky T. Q. Chen, Yulia Rubanova, Jesse Bettencourt, and David Duvenaud. Neural ordinary differential equations. In *Proceedings of the 32nd Conference on Neural Information Processing Systems*, 2018.
- Kacper Chwialkowski, Heiko Strathmann, and Arthur Gretton. A kernel test of goodness of fit. In *Proceedings of the 33rd International Conference on Machine Learning*, 2016.
- Donald L Cohn. *Measure Theory*. Springer, 2013.
- Luc Devroye. *Non-Uniform Random Variable Generation*. Springer, 2013.
- Laurent Dinh, David Krueger, and Yoshua Bengio. NICE: Non-linear independent components estimation. *arXiv:1410.8516*, 2014.
- Laurent Dinh, Jascha Sohl-Dickstein, and Samy Bengio. Density estimation using real NVP. *arXiv:1605.08803*, 2016.
- Hadi M. Dolatabadi, Sarah Erfani, and Christopher Leckie. Invertible generative modeling using linear rational splines. *arXiv:2001.05168*, 2020.
- Conor Durkan, Artur Bekasov, Iain Murray, and George Papamakarios. Neural spline flows. In *Proceedings of the 33rd Conference on Neural Information Processing Systems*, 2019.
- Gintare Karolina Dziugaite, Daniel M Roy, and Zoubin Ghahramani. Training generative neural networks via maximum mean discrepancy optimization. In *Proceedings of the 31st Conference on Uncertainty in Artificial Intelligence*, pages 258–267, 2015.
- Andreas Eberle. Reflection couplings and contraction rates for diffusions. *Probability Theory and Related Fields*, 166(3-4):851–886, Oct 2015. ISSN 1432-2064.
- Rémi Flamary and Nicolas Courty. POT: Python Optimal Transport library. <https://pythonot.github.io/>, 2017.



- Damien Garreau, Wittawat Jitkrittum, and Motonobu Kanagawa. Large sample analysis of the median heuristic, 2018.
- Mathieu Germain, Karol Gregor, Iain Murray, and Hugo Larochelle. MADE: Masked autoencoder for distribution estimation. In *Proceedings of the 32nd International Conference on Machine Learning*, 2015.
- Peter W Glynn. Stochastic approximation for Monte Carlo optimization. In *Proceedings of the 18th Winter Simulation Conference*, pages 356–365, 1986.
- Ian Goodfellow, Jean Pouget-Abadie, Mehdi Mirza, Bing Xu, David Warde-Farley, Sherjil Ozair, Aaron Courville, and Yoshua Bengio. Generative adversarial nets. In *Proceedings of the 28th Conference on Neural Information Processing Systems*, pages 2672–2680, 2014.
- Jackson Gorham and Lester Mackey. Measuring sample quality with Stein’s method. In *Proceedings of the 29th Conference on Neural Information Processing Systems*, 2015.
- Jackson Gorham and Lester Mackey. Measuring sample quality with kernels. In *Proceedings of the 34th International Conference on Machine Learning*, 2017.
- Matthew M Graham. Mici: Python implementations of manifold MCMC methods. <https://github.com/matt-graham/mici>, November 2020.
- Will Grathwohl, Kuan-Chieh Wang, Jörn-Henrik Jacobsen, David Duvenaud, and Richard Zemel. Learning the Stein discrepancy for training and evaluating energy-based models without sampling. In *Proceedings of the 37th International Conference on Machine Learning*, 2020.
- Matthew D Hoffman. Learning deep latent Gaussian models with Markov chain Monte Carlo. In *Proceedings of the 34th International Conference on Machine Learning*, pages 1510–1519, 2017.
- Matthew D Hoffman and Andrew Gelman. The No-U-Turn sampler: Adaptively setting path lengths in Hamiltonian Monte Carlo. *Journal of Machine Learning Research*, 15(1): 1593–1623, 2014.
- Tianyang Hu, Zixiang Chen, Hanxi Sun, Jincheng Bai, Mao Ye, and Guang Cheng. Stein neural sampler. *arXiv:1810.03545*, 2018.
- Chin-Wei Huang, David Krueger, Alexandre Lacoste, and Aaron Courville. Neural autoregressive flows. In *Proceedings of the 35th International Conference on Machine Learning*, 2018.
- Pavel Izmailov, Polina Kirichenko, Marc Finzi, and Andrew Gordon Wilson. Semi-supervised learning with normalizing flows. In *Proceedings of the 37th International Conference on Machine Learning*, 2020.

- Alexander Kechris. *Classical Descriptive Set Theory*. Springer, 1995.
- D. P. Kingma and M. Welling. Auto-encoding variational Bayes. In *Proceedings of the 2nd International Conference on Learning Representations*, 2013.
- Diederik P. Kingma and Jimmy Ba. Adam: A method for stochastic optimization. In *Proceedings of the 3rd International Conference on Learning Representations*, 2015.
- Durk P Kingma, Tim Salimans, Rafal Jozefowicz, Xi Chen, Ilya Sutskever, and Max Welling. Improved variational inference with inverse autoregressive flow. In *Proceedings of the 30th Conference on Neural Information Processing Systems*, 2016.
- Herbert Knothe et al. Contributions to the theory of convex bodies. *The Michigan Mathematical Journal*, 4(1):39–52, 1957.
- Ivan Kobyzev, Simon Prince, and Marcus Brubaker. Normalizing flows: An introduction and review of current methods. *IEEE Transactions on Pattern Analysis and Machine Intelligence*, 2020. ISSN 1939-3539. URL <http://dx.doi.org/10.1109/TPAMI.2020.2992934>. To appear.
- Harold Kushner and G. George Yin. *Stochastic Approximation and Recursive Algorithms and Applications*. Springer Science & Business Media, 2003.
- Pierre L’Ecuyer. Note: On the interchange of derivative and expectation for likelihood ratio derivative estimators. *Management Science*, 41:738–747, 04 1995. doi: 10.1287/mnsc.41.4.738.
- Yujia Li, Kevin Swersky, and Rich Zemel. Generative moment matching networks. In *Proceedings of the 32nd International Conference on Machine Learning*, pages 1718–1727, 2015.
- Qiang Liu and Dilin Wang. Stein variational gradient descent: A general purpose Bayesian inference algorithm. In *Proceedings of the 30th Conference on Neural Information Processing Systems*, 2016.
- Qiang Liu, Jason D. Lee, and Michael I. Jordan. A kernelized Stein discrepancy for goodness-of-fit tests and model evaluation. In *Proceedings of the 33rd International Conference on Machine Learning*, 2016.
- Samuel Livingstone and Giacomo Zanella. On the robustness of gradient-based MCMC algorithms. *arXiv:1908.11812*, 2019.
- Youssef Marzouk, Tarek Moselhy, Matthew Parno, and Alessio Spantini. Sampling via Measure Transport: An Introduction. *Handbook of Uncertainty Quantification*, page 1–41, 2016.

- George Papamakarios, Eric Nalisnick, Danilo Jimenez Rezende, Shakir Mohamed, and Balaji Lakshminarayanan. Normalizing flows for probabilistic modeling and inference. *arXiv:1912.02762*, 2019.
- Matthew D Parno and Youssef M Marzouk. Transport map accelerated Markov chain Monte Carlo. *SIAM/ASA Journal on Uncertainty Quantification*, 6(2):645–682, 2018.
- Guilherme G. P. Freitas Pires and Mário A. T. Figueiredo. Variational mixture of normalizing flows. *arXiv:2009.00585*, 2020.
- Dennis Prangle. Distilling importance sampling. *arXiv:1910.03632*, 2019.
- Rajesh Ranganath, Dustin Tran, Jaan Altosaar, and David Blei. Operator variational inference. In *Proceedings of the 30th Annual Conference on Neural Information Processing Systems*, pages 496–504, 2016.
- Danilo Jimenez Rezende and Shakir Mohamed. Variational inference with normalizing flows. 2015.
- Danilo Jimenez Rezende, Shakir Mohamed, and Daan Wierstra. Stochastic backpropagation and variational inference in deep latent Gaussian models. In *Proceedings of the 31st International Conference on Machine Learning*, 2014.
- Herbert Robbins and Sutton Monro. A stochastic approximation method. *The Annals of Mathematical Statistics*, 22(3):400–407, 09 1951. URL <https://doi.org/10.1214/aoms/1177729586>.
- Larry L. Rockwood. *Introduction to Population Ecology*. Wiley-Blackwell, 2015. ISBN 978-1-118-94757-9.
- Murray Rosenblatt. Remarks on a multivariate transformation. *The Annals of Mathematical Statistics*, 23(3):470–472, 1952.
- Sebastian Ruder. An overview of gradient descent optimization algorithms. *arXiv:1609.04747*, 2016.
- Tim Salimans, Diederik Kingma, and Max Welling. Markov chain Monte Carlo and variational inference: Bridging the gap. In *Proceedings of the 32nd International Conference on Machine Learning*, pages 1218–1226, 2015.
- Charles Stein. A bound for the error in the normal approximation to the distribution of a sum of dependent random variables. In *Proceedings of the Sixth Berkeley Symposium on Mathematical Statistics and Probability, Volume 2: Probability Theory*, pages 583–602, Berkeley, Calif., 1972. University of California Press. URL <https://projecteuclid.org/euclid.bsmmsp/1200514239>.

- Annett B. Sullivan, Dean M. Snyder, and Stewart A. Rounds. Controls on biochemical oxygen demand in the upper Klamath river, Oregon. *Chemical Geology*, 269(1):12 – 21, 2010. ISSN 0009-2541. doi: <https://doi.org/10.1016/j.chemgeo.2009.08.007>. URL <http://www.sciencedirect.com/science/article/pii/S0009254109003404>.
- Achille Thin, Nikita Kotelevskii, Jean-Stanislas Denain, Leo Grinsztajn, Alain Durmus, Maxim Panov, and Eric Moulines. MetFlow: A new efficient method for bridging the gap between Markov chain Monte Carlo and variational inference. *arXiv:2002.12253*, 2020.
- Alexandre B. Tsybakov. *Introduction to Nonparametric Estimation*. Springer Series in Statistics. Springer, 2009. ISBN 978-0-387-79052-7.
- Cedric Villani. *Optimal Transport, Old and New*. Springer, 2009.
- Li K Wenliang. Blindness of score-based methods to isolated components and mixing proportions. *arXiv:2008.10087*, 2020.
- Florian Wenzel, Alexander Buchholz, and Stephan Mandt. Quasi-Monte Carlo flows. In *Proceedings of the 3rd Workshop on Bayesian Deep Learning*, 2018.
- Christopher Wolf, Maximilian Karl, and Patrick van der Smagt. Variational inference with Hamiltonian Monte Carlo. *arXiv:1609.08203*, 2016.

# Supplement

This supplement is structured as follows:

- Appendix A contains the proofs of the theory developed in the main text: Proposition 1 (Appendix A.1), Proposition 2 (Appendix A.2), Theorem 2 (Appendix A.3) and Proposition 3 (Appendix A.4).
- Appendix B contains the computational details and extensions to the experiments detailed in Section 4. Appendix B.1 explains how the Wasserstein-1 distance was computed as our performance metric. Appendix B.2 provides the full details of the synthetic test-bed experiments used in Section 4.1. Similarly, Appendix B.3 and Appendix B.4 provides the full details of the biochemical oxygen demand experiment of Section 4.2 and Section 4.3 respectively.
- Appendix C contains further investigations into the methods presented in the main paper. Appendix C.1 discusses the sensitivity to initialisation and explains how the transport maps were initialised for the experiments of Section 4. Appendix C.2 explores variations on the stochastic optimisation method. Appendix C.3 explores the use of quasi Monte Carlo in the stochastic approximation of gradients for KSD. In Appendix C.4, we investigate the effect of the changing the reference distribution. In Appendix C.5, we explore the effect of the length-scale parameter  $\ell$  on KSD-based measure transport. Appendix C.6 explores the effect of the input dimension in the ReLU network transport map. In Appendix C.7, we investigate KSD-based measure transport using a (biased) V-statistic estimator of KSD against the unbiased U-statistic estimator that was used for the experiments presented in the main text. Finally, in Appendix C.8, we document certain pathological behaviours experienced when using KSD for measure transport and offer potential remedies.

## A Proof of Theoretical Results

This section contains the proofs for all novel theoretical results stated in the main text. In Appendix A.1 we present the proof of Proposition 1; in Appendix A.2 we present the proof of Proposition 2; the proof of Theorem 2 is contained in Appendix A.3, and finally, the proof of Proposition 3 is in Appendix A.4.

### A.1 Proof of Proposition 1

The argument involved in the proof of Proposition 1 requires differentiation under an integral. The measure-theoretic calculus result that we exploit to justify the interchange of differentiation and integration (Lemma 2 below) requires the following mathematical concepts:

**Definition 2.** Let  $\Omega$  be a measurable space and let  $\Theta$  be a topological space. A function  $f : \Theta \times \Omega \rightarrow \mathbb{R}$  is a Carathéodory function if for each  $\theta \in \Theta$  the map  $\omega \mapsto f(\theta, \omega)$  is measurable and for each  $\omega \in \Omega$  the map  $\theta \mapsto f(\theta, \omega)$  is continuous.

**Definition 3.** Let  $\Omega$  be a measurable space equipped with a measure  $\mu$  and let  $\Theta$  be a topological space. A function  $f : \Theta \times \Omega \rightarrow \mathbb{R}$  is locally uniformly integrably bounded if for every  $\theta \in \Theta$  there is a non-negative measurable function  $h_\theta : \Omega \rightarrow \mathbb{R}$  such that  $\int_\Omega h_\theta(\omega) d\mu(\omega) < \infty$ , and there exists a neighbourhood  $U_\theta$  of  $\theta$  such that for all  $\vartheta \in U_\theta$  we have  $|f(\vartheta, \omega)| \leq h_\theta(\omega)$ .

The following sufficient condition for a function to be locally uniformly integrably bounded will be used:

**Lemma 1.** In the setting of Definition 3, let  $\Theta \subseteq \mathbb{R}^d$  be an open set and assume further that, for each  $\omega \in \Omega$ , the function  $\theta \mapsto f(\theta, \omega)$  is continuous and that, for each  $\theta \in \Theta$ , the integral  $\int_\Omega |f(\theta, \omega)| d\mu(\omega) < \infty$  exists. Then  $f$  is locally uniformly integrably bounded.

*Proof.* Fix  $\theta \in \Theta$  and  $\omega \in \Omega$ . Since  $f(\theta, \omega)$  is continuous in  $\theta$  and  $\Theta$  is open, we can find a neighbourhood  $U_\theta$  of  $\theta$  on which  $f(\vartheta, \omega) \leq f(\theta, \omega) + 1$  for all  $\vartheta \in U_\theta$ . Take  $h_\theta(\omega) := |f(\theta, \omega)| + 1$ , recalling that the absolute value of a measurable function is measurable and sums of measurable functions are measurable. Then  $\int_\Omega h_\theta(\omega) d\mu(\omega) = \int_\Omega |f(\theta, \omega)| d\mu(\omega) + 1 < \infty$  and  $|f(\vartheta, \omega)| \leq h_\theta(\omega)$ , as required.  $\square$

**Lemma 2** (Differentiate under the integral). Let  $\Omega$  be a measurable space equipped with a measure  $\mu$ , let  $\Theta \subseteq \mathbb{R}^d$  be an open set and let  $f : \Theta \times \Omega \rightarrow \mathbb{R}$  be a Carathéodory function. Assume further that  $f$  is locally uniformly integrably bounded and that, for each  $i$  and each  $\omega$ , the function  $\theta \mapsto \partial_{\theta_i} f(\theta, \omega)$  is locally uniformly integrably bounded. Then the function  $g : \Theta \rightarrow \mathbb{R}$  defined by

$$g(\theta) := \int_\Omega f(\theta, \omega) d\mu(\omega)$$

is continuously differentiable and

$$\nabla_\theta g(\theta) = \int_\Omega \nabla_\theta f(\theta, \omega) d\mu(\omega).$$

*Proof.* This standard result can be found, for example, in Aliprantis and Burkinshaw [1998, Theorem 24.5, p.193], Billingsley [1979, Theorem 16.8, pp.181–182], with the statement here based on the account in Border [2016].  $\square$

The proof of Proposition 1 can now be presented:

*Proof of Proposition 1.* Using (5) and the reparametrisation trick [Glynn, 1986, L'Ecuyer, 1995, Kingma and Welling, 2013]:

$$\begin{aligned} \nabla_\theta [\mathcal{D}_S(P, T_\#^\theta Q)^2] &= \nabla_\theta \mathbb{E}_{Y, Y' \sim T_\#^\theta Q} [u_p(Y, Y')] \\ &= \nabla_\theta \mathbb{E}_{X, X' \sim Q} [u_p(T^\theta(X), T^\theta(X'))] \end{aligned} \tag{13}$$

From Lemma 2, the preconditions of Proposition 1 justify the interchange of the derivative and the expectation in (13). Indeed, in the setting of Lemma 2 we identify  $\Omega = \mathcal{X} \times \mathcal{X}$ ,  $\mu = Q \times Q$  and  $f(\theta, \omega) = u_p(T^\theta(x), T^\theta(x'))$  where  $\omega = (x, x')$ . That  $f$  is a Carathéodory function follows from (A1) and (A4) of Proposition 1, where we note that (A4) implies  $\theta \mapsto \nabla_\theta u_p(T^\theta(x), T^\theta(x'))$  is continuous. That  $f$  is locally uniformly integrably bounded follows from assumptions (A2) and (A4) together with Lemma 1. Similarly, that  $\partial_{\theta_i} f$  is locally uniformly integrably bounded follows from assumptions (A3) and (A4) together with Lemma 1. Thus the preconditions of Lemma 2 hold.

Interchanging the derivative with the expectation gives that

$$\begin{aligned} \nabla_\theta [\mathcal{D}_S(P, T_\#^\theta Q)^2] &= \mathbb{E}_{X, X' \sim Q} [\nabla_\theta u_p(T^\theta(X), T^\theta(X'))] \\ &= \mathbb{E} \left[ \frac{1}{n(n-1)} \sum_{i \neq j}^n \nabla_\theta u_p(T^\theta(x_i), T^\theta(x_j)) \right], \end{aligned}$$

as claimed.  $\square$

Note that we presented stronger conditions in Proposition 1 than are required. This was to control the length of the main text, but it is immediately clear from the proof of Proposition 1 that these conditions can be weakened to those that are required for Lemma 2 to hold.

## A.2 Proof of Proposition 2

First we present an existence result in Proposition 4, before considering regularity of the associated transport map. Recall that in this paper all measurable spaces  $\mathcal{X}$  and  $\mathcal{Y}$  are equipped with their respective Borel  $\sigma$ -algebras  $\Sigma_{\mathcal{X}}$  and  $\Sigma_{\mathcal{Y}}$ . A separable complete metric space equipped with its Borel  $\sigma$ -algebra is called a *standard Borel space*. A measure  $Q \in \mathcal{P}(\mathcal{X})$  is said to be *continuous* if  $Q(\{x\}) = 0$  for all  $x \in \mathcal{X}$ . A map  $f : \mathcal{X} \rightarrow \mathcal{Y}$  is called a *Borel isomorphism* if  $f$  is a bijection and both  $f$  and  $f^{-1}$  are Borel measurable. A fundamental result that we will exploit is known as the *isomorphism theorem for measures*:

**Theorem 3** (Isomorphism Theorem). *Let  $\mathcal{X}$  be a standard Borel space and  $Q \in \mathcal{P}(\mathcal{X})$  be continuous. Then there is a Borel isomorphism  $f : \mathcal{X} \rightarrow [0, 1]$  with  $f_\# Q = m|_{[0,1]}$ , where  $m|_{[0,1]}$  is the Lebesgue measure restricted to  $[0, 1]$ .*

*Proof.* This result can be found as Theorem 17.41 in Kechris [1995].  $\square$

**Proposition 4.** *Suppose that  $\mathcal{X}$  and  $\mathcal{Y}$  are separable complete metric spaces and suppose that  $Q \in \mathcal{P}(\mathcal{X})$  and  $P \in \mathcal{P}(\mathcal{Y})$  are such that  $Q(\{x\}) = 0$  and  $P(\{y\}) = 0$  for all  $x \in \mathcal{X}$  and  $y \in \mathcal{Y}$ . Then there exists a measurable function  $T : \mathcal{X} \rightarrow \mathcal{Y}$  such that  $T_\# Q = P$ .*

*Proof.* Our assumptions imply that  $\mathcal{X}, \mathcal{Y}$  are standard Borel spaces and  $Q \in \mathcal{P}(\mathcal{X})$ ,  $P \in \mathcal{P}(\mathcal{Y})$  are continuous. Thus from Theorem 3, there exists a Borel isomorphism  $f : \mathcal{X} \rightarrow [0, 1]$  such that  $f_\# Q = m|_{[0,1]}$  and a Borel isomorphism  $g : \mathcal{Y} \rightarrow [0, 1]$  such that  $g_\# P = m|_{[0,1]}$ . Then  $T := g^{-1} \circ f : \mathcal{X} \rightarrow \mathcal{Y}$  is measurable and satisfies  $T_\# Q = P$ , as required.  $\square$

Now we can present the proof of Proposition 2.

*Proof of Proposition 2.* Assumption 1 ensures that  $\mathcal{X}$  is a separable complete metric space and  $Q(\{x\}) = 0$  for all  $x \in \mathcal{X}$ . Assumption 2 restricts attention to  $\mathcal{Y} = \mathbb{R}^d$ , meaning that  $\mathcal{Y}$  is a separable complete metric space, and requires  $P$  to admit a density on  $\mathcal{Y}$ , meaning that  $P(\{y\}) = 0$  for all  $y \in \mathcal{Y}$ . Thus the existence of a transport map  $T$  from  $Q$  to  $P$  is guaranteed by Proposition 4.

It remains to show that, for *any* such transport map,  $T \in \prod_{i=1}^d L^2(Q)$ . To this end, we have that

$$\begin{aligned} \|T\|_{\prod_{i=1}^d L^2(Q)}^2 &= \sum_{i=1}^d \|T_i\|_{L^2(Q)}^2 = \sum_{i=1}^d \int_{\mathcal{X}} T_i(x)^2 dQ(x) = \int_{\mathcal{X}} \|T(x)\|^2 dQ(x) \\ &\stackrel{(*)}{=} \int_{\mathbb{R}^d} \|x\|^2 d(T_{\#}Q)(x) = \int_{\mathbb{R}^d} \|x\|^2 dP(x) < \infty, \end{aligned}$$

where a change of variables was used at  $(*)$  and the final inequality follows from the assumption that  $P \in \mathcal{P}_2(\mathbb{R}^d)$  in Assumption 2.  $\square$

### A.3 Proof of Theorem 2

Recall that for  $P, P' \in \mathcal{P}_1(\mathbb{R}^d)$  the (first) *Wasserstein distance* is defined as [Villani, 2009, Remark 6.5]

$$W_1(P, P') := \sup_{f \in \mathcal{F}} |\mathbb{E}_{Y \sim P}[f(Y)] - \mathbb{E}_{Y \sim P'}[f(Y)]|, \quad (14)$$

where  $\mathcal{F} := \{f : \mathbb{R}^d \rightarrow \mathbb{R} \mid \|f\|_L \leq 1\}$  and  $\|f\|_L := \sup_{x \neq y} \frac{|f(x) - f(y)|}{\|x - y\|}$  is the Lipschitz seminorm on  $\mathbb{R}^d$ . Our proof of Theorem 2 is based on the following result that relates convergence in  $W_1$  to convergence in KSD:

**Proposition 5** (Wasserstein Controls KSD). *Let  $k : \mathbb{R}^d \times \mathbb{R}^d \rightarrow \mathbb{R}$  be symmetric positive definite with  $(x, y) \mapsto k(x, y)$ ,  $(x, y) \mapsto \partial_{x_i} \partial_{y_i} k(x, y)$  and  $(x, y) \mapsto \partial_{x_i} \partial_{x_j} \partial_{y_i} \partial_{y_j} k(x, y)$  continuous and bounded for all  $i, j \in \{1, \dots, d\}$ . Let  $P \in \mathcal{P}(\mathbb{R}^d)$  admit a density function  $p$  such that  $\nabla \log p$  is Lipschitz with  $\mathbb{E}_{X \sim P}[\|\nabla \log p(X)\|_2^2] < \infty$ . Let  $\mathcal{D}_S$  denote the KSD based on  $P$  and  $k$ , as defined in (7). Then a sequence  $(Q_n)_{n \in \mathbb{N}} \subset \mathcal{P}(\mathbb{R}^d)$  satisfies  $\mathcal{D}_S(P, Q_n) \rightarrow 0$  whenever  $W_1(P, Q_n) \rightarrow 0$ .*

*Proof.* This result is Proposition 9 of Gorham and Mackey [2017].  $\square$

Recall that in this paper  $\mathcal{X}$  is always assumed to be a Borel space. The following result is also required:

**Lemma 3** ( $L^2$  Controls Wasserstein). *Let  $Q \in \mathcal{P}(\mathcal{X})$  and let  $S, T \in \prod_{i=1}^d L^2(Q)$ . Then we have the bound  $W_1(S_{\#}Q, T_{\#}Q) \leq \|S - T\|_{\prod_{i=1}^d L^2(Q)}$ .*



*Proof.* From the definition of the (first) Wasserstein distance, we have

$$\begin{aligned} W_1(S_{\#}Q, T_{\#}Q) &= \sup_{\|f\|_L \leq 1} \left| \int_{\mathcal{X}} f(x) dS_{\#}Q(x) - \int_{\mathcal{X}} f(x) dT_{\#}Q(x) \right| \\ &= \sup_{\|f\|_L \leq 1} \left| \int_{\mathcal{X}} f(S(x)) - f(T(x)) dQ(x) \right|. \end{aligned}$$

If  $\|f\|_L \leq 1$  then  $|f(a) - f(b)| \leq \|a - b\|$  for all  $a, b \in \mathbb{R}^d$ , and so

$$\begin{aligned} W_1(S_{\#}Q, T_{\#}Q) &\leq \int_{\mathcal{X}} \|S(x) - T(x)\| dQ(x) \\ &\leq \left( \int_{\mathcal{X}} \|S(x) - T(x)\|^2 dQ(x) \right)^{1/2} = \|S - T\|_{\prod_{i=1}^d L^2(Q)} \end{aligned}$$

where the second inequality is Jensen's inequality.  $\square$

Our final ingredient is a basic result on the inverse multi-quadric kernel:

**Lemma 4** (Derivatives of the Inverse Multi-quadric Kernel). *The inverse multi-quadric kernel in (3),  $k(x, y) = (c^2 + \|x - y\|^2)^{\beta}$ , with  $c > 0$  and  $\beta \in (-1, 0)$ , satisfies*

$$\sup_{x, y \in \mathbb{R}^d} \left| \partial_{x_1}^{\alpha_1} \dots \partial_{x_d}^{\alpha_d} \partial_{y_1}^{\alpha_1} \dots \partial_{y_d}^{\alpha_d} k(x, y) \right| < \infty$$

for all multi-indices  $\alpha = (\alpha_1, \dots, \alpha_d) \in \mathbb{N}_0^d$ .

*Proof.* For  $\alpha \in \mathbb{N}_0^d$  let  $|\alpha| := \alpha_1 + \dots + \alpha_d$ . Recall that a polynomial  $\prod_{|\alpha| \leq s} c_{\alpha} z_1^{\alpha_1} \dots z_d^{\alpha_d}$  is said to have *maximal degree*  $s$ , where  $s = |\alpha|$  is the largest integer for which  $c_{\alpha} \neq 0$  for some  $\alpha \in \mathbb{N}_0^d$ . Let

$$\mathcal{F} := \left\{ (x, y) \mapsto k(x, y) \frac{r_m(x - y)}{(c^2 + \|x - y\|^2)^m} : r_m \text{ is a polynomial of maximal degree } 2m, m \in \mathbb{N}_0 \right\}.$$

Then  $k(x, y) \in \mathcal{F}$  and  $\mathcal{F}$  is closed under the action of each of the differential operators  $\partial_{x_i} \partial_{y_i}$ ,  $i \in \{1, \dots, d\}$ . Indeed, we have from the product rule that

$$\partial_{x_i} \left[ k(x, y) \frac{r_m(x - y)}{(c^2 + \|x - y\|^2)^m} \right] = \frac{2\beta(x_i - y_i)k(x, y)r_m(x - y)}{(c^2 + \|x - y\|^2)^{m+1}} + \frac{k(x, y)\partial_{x_i}r_m(x - y)}{(c^2 + \|x - y\|^2)^m} - \frac{2m(x_i - y_i)k(x, y)r_m(x - y)}{(c^2 + \|x - y\|^2)^{m+1}}$$

and

$$\begin{aligned} \partial_{x_i} \partial_{y_i} \left[ k(x, y) \frac{r_m(x - y)}{(c^2 + \|x - y\|^2)^m} \right] &= \left[ -\frac{2\beta k(x, y)r_m(x - y)}{(c^2 + \|x - y\|^2)^{m+1}} - \frac{4\beta^2(x_i - y_i)^2 k(x, y)r_m(x - y)}{(c^2 + \|x - y\|^2)^{m+2}} \right. \\ &\quad \left. + \frac{2\beta(x_i - y_i)k(x, y)\partial_{y_i}r_m(x - y)}{(c^2 + \|x - y\|^2)^{m+1}} + \frac{4(m+1)\beta(x_i - y_i)^2 k(x, y)r_m(x - y)}{(c^2 + \|x - y\|^2)^{m+2}} \right] \\ &\quad + \left[ -\frac{2\beta(x_i - y_i)k(x, y)\partial_{x_i}r_m(x - y)}{(c^2 + \|x - y\|^2)^{m+1}} + \frac{k(x, y)\partial_{x_i}\partial_{y_i}r_m(x - y)}{(c^2 + \|x - y\|^2)^m} \right] \end{aligned}$$

$$\begin{aligned}
& + \frac{2m(x_i - y_i)k(x, y)\partial_{x_i}r_m(x - y)}{(c^2 + \|x - y\|^2)^{m+1}} \Big] \\
& + \left[ \frac{2mk(x, y)r_m(x - y)}{(c^2 + \|x - y\|^2)^{m+1}} + \frac{4\beta m(x_i - y_i)^2 k(x, y)r_m(x - y)}{(c^2 + \|x - y\|^2)^{m+2}} \right. \\
& \quad \left. - \frac{2m(x_i - y_i)k(x, y)\partial_{y_i}r_m(x - y)}{(c^2 + \|x - y\|^2)^{m+1}} + \frac{4m(m+1)(x_i - y_i)^2 k(x, y)r_m(x - y)}{(c^2 + \|x - y\|^2)^{m+2}} \right] \\
& = k(x, y) \frac{r_{m+2}(x - y)}{(c^2 + \|x - y\|^2)^{m+2}} \tag{15}
\end{aligned}$$

where  $r_{m+2}(x - y)$  has been implicitly defined. Since  $\partial_{x_i}(x_i - y_i)^s = s(x_i - y_i)^{s-1}$ , it follows that the terms  $\partial_{x_i}r_m(x - y)$ ,  $\partial_{y_i}r_m(x - y)$  and  $\partial_{x_i}\partial_{y_i}r_m(x - y)$  appearing in (15) are polynomials in  $x - y$  of maximal degree  $2m$ . Thus, from (15),  $r_{m+2}(x - y)$  is a polynomial of maximal degree  $2(m + 2)$ , showing that the set  $\mathcal{F}$  is closed under the action of  $\partial_{x_i}\partial_{y_i}$ .

Since the differential operator  $\partial_{x_1}^{\alpha_1} \dots \partial_{x_d}^{\alpha_d}$  is obtained by repeated application of operators of the form  $\partial_{x_i}\partial_{y_i}$ , and since it is clear that all elements of  $\mathcal{F}$  are bounded on  $\mathbb{R}^d \times \mathbb{R}^d$ , the claim is established.  $\square$

Now we can prove Theorem 2:

*Proof of Theorem 2.* First note that our preconditions are a superset of those required for Theorem 1. Thus the conclusion of Theorem 1 holds; namely, if  $\mathcal{D}_S(P, (T_n)_\#Q) \rightarrow 0$  then  $(T_n)_\#Q \Rightarrow P$ . From (11) we have that  $\mathcal{D}_S(P, (T_n)_\#Q)$  and  $\inf_{T \in \mathcal{T}_n} \mathcal{D}_S(P, T_\#Q)$  agree in the  $n \rightarrow \infty$  limit. Thus it is sufficient to show that  $\inf_{T \in \mathcal{T}_n} \mathcal{D}_S(P, T_\#Q) \rightarrow 0$  in the  $n \rightarrow \infty$  limit.

Second, note that our preconditions are also a superset of those required for Proposition 5. Indeed, from Lemma 4 the inverse multi-quadric kernel in (3) is infinitely differentiable with derivatives of all orders bounded. Thus it is sufficient to show that  $\inf_{T \in \mathcal{T}_n} W_1(P, T_\#Q) \rightarrow 0$  in the  $n \rightarrow \infty$  limit.

From Assumptions 1 and 2 and Proposition 2, there exists a map  $T \in \prod_{i=1}^d L^2(Q)$  with  $T_\#Q = P$ . From Assumption 3, there is a set  $\mathfrak{T}$  such that  $T \in \mathfrak{T} \subseteq \prod_{i=1}^d L^2(Q)$  and the set  $\mathcal{T}_\infty$  is dense in  $\mathfrak{T}$ . Thus there exists a sequence  $(S_n)_{n \in \mathbb{N}} \subset \mathcal{T}_\infty$  with  $S_n \rightarrow T$  in  $\prod_{i=1}^d L^2(Q)$ .

For each  $n \in \mathbb{N}$ , let  $m_n \in \mathbb{N}$  denote the smallest integer  $m$  for which  $S_n \in \mathcal{T}_m$ , which is well-defined since  $S_n \in \mathcal{T}_\infty = \cup_{i \in \mathbb{N}} \mathcal{T}_i$ . Let  $M_n := \max\{m_1, \dots, m_n, n\}$ , so that  $M_n$  is a non-decreasing sequence with  $M_n \rightarrow \infty$  in the  $n \rightarrow \infty$  limit. Note that, since  $\mathcal{T}_i \subseteq \mathcal{T}_j$  for all  $i \leq j$ , we have  $S_n \in \mathcal{T}_{M_n}$ .

Thus from Lemma 3 we conclude that

$$0 \leq \inf_{T \in \mathcal{T}_{M_n}} W_1(P, T_\#Q) \leq W_1(P, (S_n)_\#Q) \leq \|T - S_n\|_{\prod_{i=1}^d L^2(Q)} \rightarrow 0 \tag{16}$$

in the  $n \rightarrow \infty$  limit. Again, since  $\mathcal{T}_i \subseteq \mathcal{T}_j$  for  $i \leq j$ , the sequence  $n \mapsto \inf_{T \in \mathcal{T}_n} W_1(P, T_\#Q)$  is non-increasing and, from (16), it has a subsequence that converges to 0. It follows that  $\lim_{n \rightarrow \infty} \inf_{T \in \mathcal{T}_n} W_1(P, T_\#Q) = 0$ , as required.  $\square$

## A.4 Proof of Proposition 3

Recall the *rectified linear unit* activation function  $\sigma(x) = \max(0, x)$ , which we consider to be applied componentwise when  $x \in \mathbb{R}^d$ .

**Definition 4** (Deep ReLU Neural Network). A deep ReLU neural network with  $l$  hidden layers from  $\mathbb{R}^p$  to  $\mathbb{R}^d$  is a function  $f : \mathbb{R}^p \rightarrow \mathbb{R}^d$  of the form

$$f = F_{l+1} \circ \sigma \circ F_l \circ \cdots \circ F_2 \circ \sigma \circ F_1$$

where  $F_i : \mathbb{R}^{w_{i-1}} \rightarrow \mathbb{R}^{w_i}$ ,  $i = 1, \dots, l$ , is an affine transformation,  $F_{l+1} : \mathbb{R}^{w_l} \rightarrow \mathbb{R}^{w_{l+1}}$  is a linear transformation,  $w_0 = p$  is the input dimension,  $w_{l+1} = d$  is the output dimension, and  $w_i \in \mathbb{N}$ ,  $i = 1, \dots, l$ , is the width of the  $i$ th hidden layer. The set of all deep ReLU neural networks with  $l$  hidden layers from  $\mathbb{R}^p$  to  $\mathbb{R}^d$  with maximum width  $\max\{w_1, \dots, w_l\} \leq n$  is denoted  $\mathcal{R}_{l,n}(\mathbb{R}^p \rightarrow \mathbb{R}^d)$  and we let  $\mathcal{R}_{l,\infty}(\mathbb{R}^p \rightarrow \mathbb{R}^d) := \lim_{n \rightarrow \infty} \mathcal{R}_{l,n}(\mathbb{R}^p \rightarrow \mathbb{R}^d)$ .

The following, essentially trivial observation will be useful:

**Proposition 6.**  $\prod_{i=1}^d \mathcal{R}_{l,\infty}(\mathbb{R}^p \rightarrow \mathbb{R}) \subset \mathcal{R}_{l,\infty}(\mathbb{R}^p \rightarrow \mathbb{R}^d)$ .

*Proof.* For fixed  $n \in \mathbb{N}$ , there is a canonical injection from  $\prod_{i=1}^d \mathcal{R}_{l,n}(\mathbb{R}^p \rightarrow \mathbb{R})$  into  $\mathcal{R}_{l,nd}(\mathbb{R}^p \rightarrow \mathbb{R}^d)$  that concatenates the  $d$  neural networks width-wise, to form a single neural network with width  $nd$ . Since every element of  $\prod_{i=1}^d \mathcal{R}_{l,\infty}(\mathbb{R}^p \rightarrow \mathbb{R})$  belongs to  $\prod_{i=1}^d \mathcal{R}_{l,n}(\mathbb{R}^p \rightarrow \mathbb{R})$  for a sufficiently large  $n \in \mathbb{N}$ , the claim is established.  $\square$

Here we introduce the shorthand  $L^2(\mathbb{R}^p)$  for  $L^2(\lambda_{\mathbb{R}^p})$  where  $\lambda_{\mathbb{R}^p}$  is the Lebesgue measure on  $\mathbb{R}^p$ . The following result on the approximation properties of deep ReLU neural networks, which derives from the fact that the set of continuous piecewise linear functions  $f : \mathbb{R} \rightarrow \mathbb{R}$  is dense in  $L^2(\mathbb{R})$ , will be required.

**Proposition 7.** For every function  $f \in \prod_{i=1}^d L^2(\mathbb{R}^p)$  and every  $\epsilon > 0$ , there exists a function  $g \in \mathcal{R}_{l,\infty}(\mathbb{R}^p \rightarrow \mathbb{R}^d)$  such that  $\|f - g\|_{\prod_{i=1}^d L^2(\mathbb{R}^p)} < \epsilon$ , where  $l = \lceil \log_2(p+1) \rceil$ .

*Proof.* For  $d = 1$ , this result is a special case of Theorem 2.3 in Arora et al. [2018], which derives from the fact that continuous piecewise linear functions are dense in  $L^2(\mathbb{R})$ .

For general  $d$ , we observe that for each component  $f_i \in L^2(\mathbb{R}^p)$  we can find a function  $g_i \in \mathcal{R}_{l,\infty}(\mathbb{R}^p \rightarrow \mathbb{R})$  with  $\|f_i - g_i\|_{L^2(\mathbb{R}^p)} < \epsilon/\sqrt{d}$ . Then, letting  $g = (g_1, \dots, g_d) : \mathbb{R}^p \rightarrow \mathbb{R}^d$ , we have that  $g \in \prod_{i=1}^d \mathcal{R}_{l,\infty}(\mathbb{R}^p \rightarrow \mathbb{R})$  and

$$\|f - g\|_{\prod_{i=1}^d L^2(\mathbb{R}^p)} = \sqrt{\sum_{i=1}^d \|f_i - g_i\|_{L^2(\mathbb{R}^p)}^2} < \sqrt{\sum_{i=1}^d \frac{\epsilon^2}{d}} = \epsilon.$$

Finally, we note from Proposition 6 that  $g \in \prod_{i=1}^d \mathcal{R}_{l,\infty}(\mathbb{R}^p \rightarrow \mathbb{R}) \subset \mathcal{R}_{l,\infty}(\mathbb{R}^p \rightarrow \mathbb{R}^d)$ .  $\square$

Now we present the proof of Proposition 3:

*Proof of Proposition 3.* From Assumptions 1 and 2 and Proposition 2 there exists  $T \in \prod_{i=1}^d L^2(Q)$  such that  $T_{\#}Q = P$ . Let  $\mathfrak{T} = \prod_{i=1}^d L^2(Q)$ , so that  $T \in \mathfrak{T}$  is satisfied.

From the statement of Proposition 3 we have  $\mathcal{T}_n := \mathcal{R}_{l,n}(\mathbb{R}^p \rightarrow \mathbb{R}^d)$  with  $l = \lceil \log_2(p+1) \rceil$ . From Definition 4 it is therefore clear that  $\mathcal{T}_n \subseteq \mathcal{T}_m$  whenever  $n \leq m$  and that  $\mathcal{T}_\infty = \mathcal{R}_{l,\infty}(\mathbb{R}^p \rightarrow \mathbb{R}^d)$ .

Thus all parts of Assumption 3 have been verified except the part that requires  $\mathcal{T}_\infty$  to be dense in  $\mathfrak{T}$ ; i.e. that the set  $\mathcal{R}_{l,\infty}(\mathbb{R}^p \rightarrow \mathbb{R}^d)$  is dense in the Hilbert space  $\prod_{i=1}^d L^2(Q)$ . To establish this last part, we will make use of Proposition 7:

Let  $T \in \prod_{i=1}^d L^2(Q)$  and  $\epsilon > 0$ . From the definition of  $L^2(Q)$ , there exists  $c \geq 0$  such that, for each of the coordinates  $i \in \{1, \dots, d\}$ ,

$$\int_{\mathbb{R}^p \setminus [-c, c]^p} T_i(x)^2 dQ(x) < \frac{\epsilon}{4d}.$$

Let

$$f_i(x) := \begin{cases} T_i(x), & x \in [-c, c]^p, \\ 0, & x \in \mathbb{R}^p \setminus [-c, c]^p. \end{cases}$$

Our assumption that  $Q$  admits a positive and continuous density  $q$  on  $\mathbb{R}^p$  ensures that  $f \in \prod_{i=1}^d L^2(\mathbb{R}^p)$ , since

$$\begin{aligned} \|f\|_{\prod_{i=1}^d L^2(\mathbb{R}^p)}^2 &= \sum_{i=1}^d \int_{[-c, c]^p} T_i(x)^2 dx = \sum_{i=1}^d \int_{[-c, c]^p} \frac{T_i(x)^2}{q(x)} dQ(x) \leq \left[ \sup_{x \in [-c, c]^d} \frac{1}{q(x)} \right] \sum_{i=1}^d \int_{[-c, c]^p} T_i(x)^2 dQ(x) \\ &\leq \left[ \sup_{x \in [-c, c]^p} \frac{1}{q(x)} \right] \sum_{i=1}^d \|T_i\|_{L^2(Q)}^2 \\ &= \left[ \sup_{x \in [-c, c]^p} \frac{1}{q(x)} \right] \|T\|_{\prod_{i=1}^d L^2(Q)}^2, \end{aligned} \tag{17}$$

where the supremum in (17) is finite, since  $q^{-1}$  is well-defined and continuous on the compact set  $[-c, c]^p$ . Let also  $q_{\max} := \sup_{x \in \mathbb{R}^p} q(x)$ , which is well-defined since we assumed  $q$  to be continuous and bounded on  $\mathbb{R}^p$ . Then, since  $f \in \prod_{i=1}^d L^2(\mathbb{R}^p)$ , we may evoke Proposition 7 to find a function  $g \in \mathcal{R}_{l,\infty}(\mathbb{R}^p \rightarrow \mathbb{R}^d)$  such that  $\|f - g\|_{\prod_{i=1}^d L^2(\mathbb{R}^p)}^2 < \epsilon/(4q_{\max})$ . It remains to check that  $g$  approximates  $T$  in  $\prod_{i=1}^d L^2(Q)$ . To this end, we can use the triangle inequality in  $\prod_{i=1}^d L^2(Q)$  and the fact that  $(a + b)^2 \leq 2(a^2 + b^2)$  to see that

$$\begin{aligned} \|T - g\|_{\prod_{i=1}^d L^2(Q)}^2 &\leq 2\|T - f\|_{\prod_{i=1}^d L^2(Q)}^2 + 2\|f - g\|_{\prod_{i=1}^d L^2(Q)}^2 \\ &= 2 \sum_{i=1}^d \int_{\mathbb{R}^p \setminus [-c, c]^p} T_i(x)^2 dQ(x) + 2 \sum_{i=1}^d \int (f_i(x) - g_i(x))^2 q(x) dx \\ &\leq 2 \sum_{i=1}^d \int_{\mathbb{R}^p \setminus [-c, c]^p} T_i(x)^2 dQ(x) + 2q_{\max} \sum_{i=1}^d \int (f_i(x) - g_i(x))^2 dx < \frac{\epsilon}{2} + \frac{\epsilon}{2} = \epsilon. \end{aligned}$$

Since  $\epsilon > 0$  was arbitrary, this argument shows that the set  $\mathcal{R}_{l,\infty}(\mathbb{R}^p \rightarrow \mathbb{R}^d)$  is dense in  $\prod_{i=1}^d L^2(Q)$ , as required.  $\square$

## B Computational Details

This section provides full details for the experiments presented in Section 4.

### B.1 Performance Metric

To estimate the Wasserstein-1 distance between the target distribution and approximations we computed the *earth mover distance* (EMD) between two uniformly weighted empirical measures, each formed from  $10^4$  samples from their respective distributions and with the Euclidean distance between the samples used to construct the cost matrix. The EMD was computed using an implementation in the Python Optimal Transport (POT) package [Flamary and Courty, 2017]. For the target distribution, independent samples were used in the synthetic test bed in Section 4.1 and thinned samples from a long HMC chain were used for the real examples in Sections 4.2 and 4.3. For the approximate distribution, independent samples from  $T_{\#}^{\theta}Q$  were used.

### B.2 Details of the Synthetic Test Bed

To assess the proposed methods, we considered the following bivariate densities

$$\begin{aligned} p_1(x, y) &:= \mathcal{N}(x; 0, \eta_1^2) \mathcal{N}(y; \sin(bx), \eta_2^2), \\ p_2(x, y) &:= \mathcal{N}(x; 0, \sigma_1^2) \mathcal{N}(y; ax^2, \sigma_2^2), \\ p_3(x, y) &:= \frac{1}{n} \sum_{i=1}^n \mathcal{N}(x, y; \mu_i, \sigma^2 I_2), \end{aligned}$$

where  $\mathcal{N}(x; \mu, \sigma^2)$  is the univariate Gaussian density with mean  $\mu$  and variance  $\sigma^2$ , and  $\mathcal{N}(x, y; \mu, K)$  is the bivariate Gaussian density with mean vector  $\mu$  and covariance matrix  $K$ . The parameter choices for the sinusoidal experiment  $p_1$  were  $\eta_1^2 = 1.3^2, \eta_2^2 = 0.001^2$  and  $b = 1.2$ . The parameter choices for the banana experiment  $p_2$  were  $\sigma_1^2 = 1, \sigma_2^2 = 0.1^2$  and  $a = 0.5$ . The parameter choices for the multi-modal experiment  $p_3$  were  $n = 4, \mu_1 = (1, 1), \mu_2 = (1, -1), \mu_3 = (-1, -1), \mu_4 = (-1, 1)$  and  $\sigma^2 = 0.2^2$ . The target densities can be seen in Figure 3.

Computational costs for each method in terms of number of target evaluations and CPU wall-clock time against performance are shown, respectively, in Figure 4 and Figure 5. From Figure 4, there is no clear sense in which KSD or KLD out-performs the other across the different synthetic tests; this is in line with the conclusion of Section 4.1. For CPU wall-clock time in Figure 5, KSD-based measure transport is approximately three to five times slower than its KLD counterpart. However, note that our implementation of KSD is not production code and further performance gains can certainly be achieved.

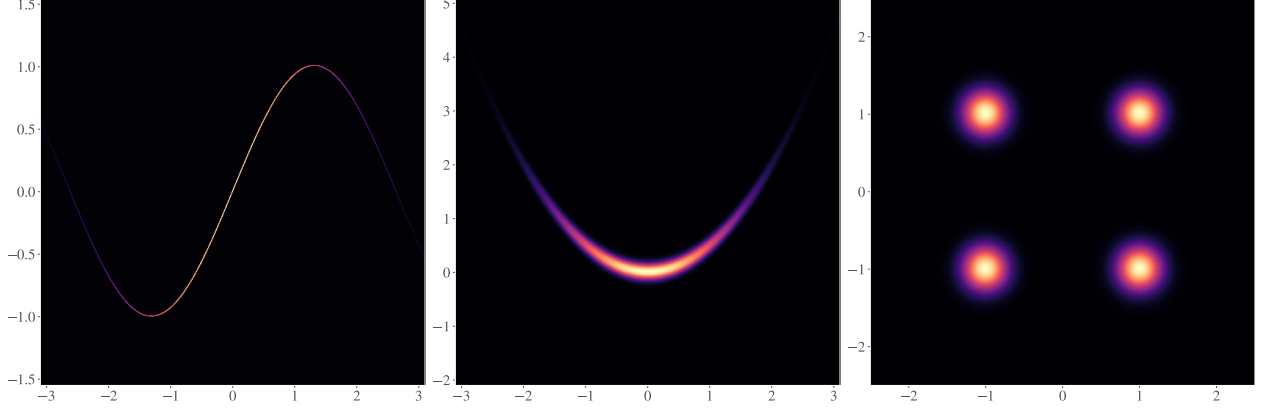


Figure 3: Contour plots of the three synthetic test densities  $p_1$ ,  $p_2$  and  $p_3$  from left to right used in Section 4.1.

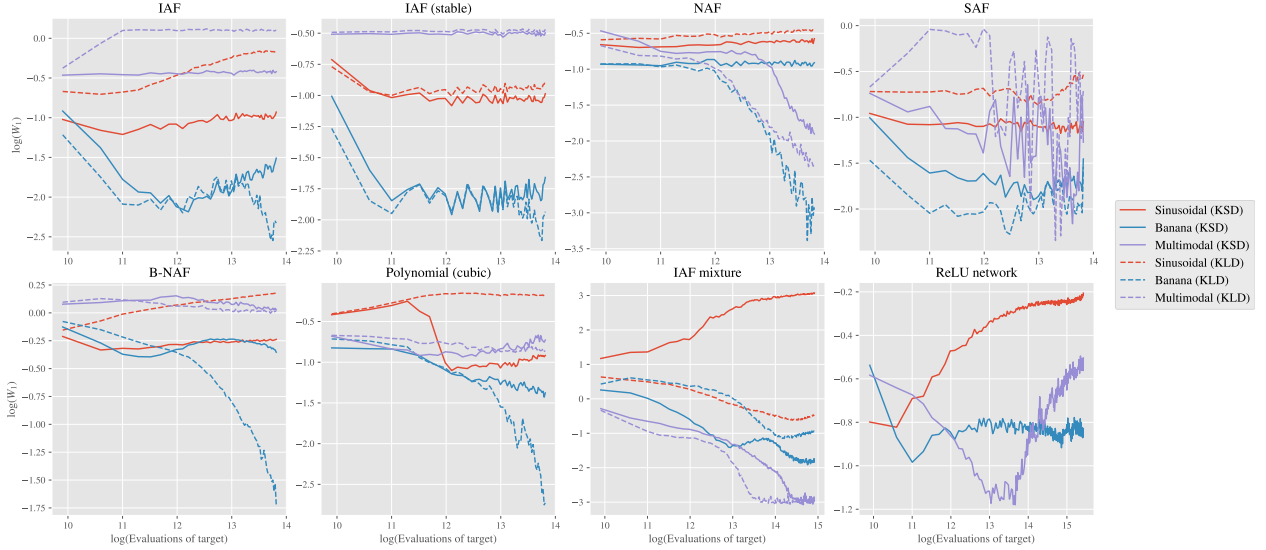


Figure 4: Wasserstein-1 metric,  $W_1$ , as a function of the total number of evaluations of either  $p$  or its gradient, for each synthetic test experiment.

We now discuss the implementations details of all the methods used in Section 4.1. In all our measure transport implementations, unless specified otherwise, we used existing implementations in Pyro [Bingham et al., 2018]. Furthermore, the reference measure used for synthetic tests was the standard Gaussian on  $\mathbb{R}^p$ .

**Hamiltonian Monte Carlo:** We used an adaptive HMC algorithm in which the integrator step size was automatically adjusted using a dual-averaging algorithm in a warm-up phase to give an average acceptance statistic of 0.8 [Betancourt et al., 2014] and the number of integrator steps per transition was set dynamically by expanding the trajectory until a termination criterion was met [Hoffman and Gelman, 2014, Betancourt, 2017]. We used

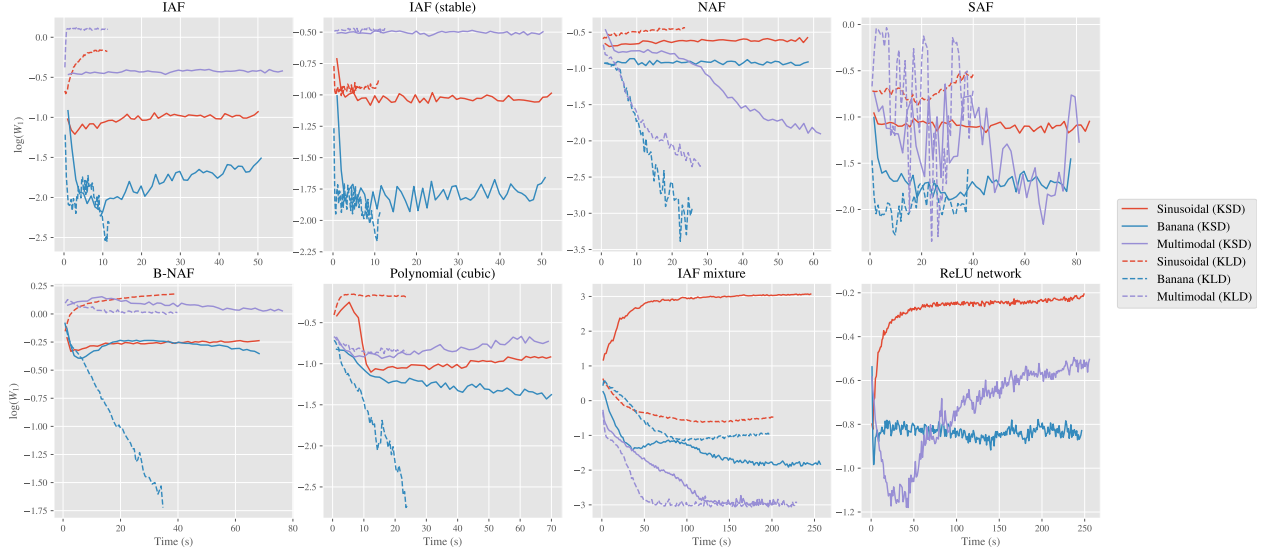


Figure 5: Wasserstein-1 metric,  $W_1$ , as a function of the CPU wall-clock time for each synthetic test experiment.

the HMC implementations in the Python package [Graham, 2020], with the dual-averaging adaptation algorithm settings following the defaults used in Stan [Carpenter et al., 2017]. Only the post-warm-up samples were included in estimates of the discrepancies and density plots.

In the following, the autoregressive neural networks that we specify are the Masked Autoencoders for Density Estimation (MADE) of Germain et al. [2015]; the only difference being, that there is no sigmoidal non-linearity applied to the output layer.

**Inverse Autoregressive Flow (IAF):** Recall from Section 2.5, that an autoregressive flow  $T : \mathbb{R}^d \rightarrow \mathbb{R}^d$  is of the form  $T_i(x) = \tau(c_i(x_1, \dots, x_{i-1}), x_i)$ , where  $T = (T_1, \dots, T_d)$  and  $x = (x_1, \dots, x_d)$ . The IAF flow of Kingma et al. [2016] takes  $c_i$  to be the  $i$ th output of an autoregressive neural network and  $\tau$  to be an affine transform of the form

$$\tau(c_i(x_1, \dots, x_{i-1}), x_i) = \mu_i + \exp(s_i)x_i,$$

where  $\mu_i \in \mathbb{R}$  and  $s_i \in \mathbb{R}$  are outputs from  $c_i(x_1, \dots, x_{i-1})$ . Note that the coefficient of  $x_i$  is forced to be positive, this ensures the resulting transport map is monotonic.

For each synthetic test problem, we used a single IAF where the dimensionality of the hidden units in the single hidden layer of the underlying autoregressive neural network was 40. The underlying autoregressive neural network used the ReLU activation function. The IAF was initialised using the same default random initialisation in both the KSD and KLD experiments. 10,000 iterations of Adam were used, with learning rate 0.001.

**Stable Inverse Autoregressive Flow (IAF stable):** Closely related to an IAF, a stable IAF was introduced in Kingma et al. [2016] in order to improve numerical stability. The

only difference being that the  $\tau$  is of the form

$$\tau(c_i(x_1, \dots, x_{i-1}), x_i) = \text{sigmoid}(s_i)x_i + (1 - \text{sigmoid}(s_i))\mu_i,$$

where  $\mu_i \in \mathbb{R}$  and  $s_i \in \mathbb{R}$  are outputs from  $c_i(x_1, \dots, x_{i-1})$  and

$$\text{sigmoid}(x) = \frac{e^x}{1 + e^x},$$

where, for  $x \in \mathbb{R}^d$ , we consider sigmoid to be applied component-wise. Since sigmoid is monotonic, the resulting transport map is again monotonic. The restriction  $\text{sigmoid}(s_i) \in (0, 1)$  may limit the expressibility of the transport map compared to standard IAF, but this at the expense of increased numerical stability.

For each synthetic test problem, we used a single stable IAF where the dimensionality of the hidden units in the single hidden layer of the underlying autoregressive neural network was 40. The underlying autoregressive neural network used the ReLU activation function. The stable IAF was initialised using the same default random initialisation in both the KSD and KLD experiments. 10,000 iterations of Adam were used, with learning rate 0.001.

**Neural Autoregressive Flow (NAF):** A NAF, introduced in Huang et al. [2018], is again an autoregressive flow which, compared to the preceding IAF and stable IAF, offers greater flexibility and a universality guarantee. The autoregressive conditioner  $c$  is again taken as an autoregressive neural network and  $\tau : \mathbb{R} \rightarrow \mathbb{R}$  takes the form of a monotonic neural network whose weights and biases are the output of the conditioner  $c$ . Monotonicity of  $\tau$  is guaranteed by using strictly positive weights and strictly monotonic activation functions.

The particular implementation of  $\tau$  that we used in Pyro uses what is termed a *deep sigmoidal flow* (DSF) in Huang et al. [2018]. A DSF is a single layer dense neural network with a sigmoidal activation function. Furthermore, in order to increase the effective range of  $\tau$ , an inverse sigmoid function is taken on the output layer. However, this inverse sigmoid function has domain  $(0, 1)$  and thus the weights and biases of the output layer must be constrained such that this composition can be well defined. In a DSF, this is achieved by having no bias term on the output layer and constraining the output layer’s weights,  $w_{ij}$ , to satisfy  $\sum_i w_{ij} = 1$ . Thus the output term of a DSF is a convex combination of the output of the hidden layer. The overall transformation of a DSF is thus of the form

$$f_{\text{DSF}} = \text{sigmoid}^{-1} \circ C \circ \text{sigmoid} \circ F$$

where  $F : \mathbb{R} \rightarrow \mathbb{R}^k$  is an affine transformation and  $C : \mathbb{R}^k \rightarrow \mathbb{R}$  is a convex combination. 10,000 iterations of Adam were used, with learning rate 0.001.

Following Huang et al. [2018], for each synthetic test problem, we used a single DSF style NAF, where the dimensionality of the hidden sigmoid units in each DSF was 16 and the dimensionality of the hidden units in the single hidden layer of the underlying autoregressive neural network was 40. The underlying autoregressive neural network used the ReLU activation function. Note that the dimensionality of  $i$ th output  $c_i$  of this autoregressive neural network is 48, due to the  $2 \times 16$  weight terms and the 16 bias terms in each DSF. The NAF was initialised using the same default random initialisation in both the KSD and KLD experiments.



**Spline Autoregressive Flow (SAF):** A SAF, developed in Durkan et al. [2019] and Dolatabadi et al. [2020], is again an autoregressive flow that takes  $\tau : \mathbb{R} \rightarrow \mathbb{R}$  as a piecewise monotonic rational polynomial function (a spline) on an interval  $[-a, a]$  and the identity otherwise. A rational polynomial function is the ratio of two polynomials. In Durkan et al. [2019], the polynomial was taken as quadratic polynomial and in Dolatabadi et al. [2020], the polynomial was taken as a linear polynomial. The parameters controlling each rational polynomial function, are the output of an autoregressive neural network. We also note that originally the spline transform was implemented in the context of coupling flows, rather than autoregressive flows.

For each synthetic test problem, we used a single SAF based on rational linear splines with 8 pieces defined on the interval  $[-3, 3]$ . The underlying autoregressive neural network had two hidden layers, each of dimension 20. The SAF was initialised using the same default random initialisation in both the KSD and KLD experiments. 10,000 iterations of Adam were used, with learning rate 0.001.

**Block Neural Autoregressive Flow (B-NAF):** A B-NAF, introduced in Cao et al. [2019], is similar in spirit to the NAF. It is an autoregressive flow, where  $\tau$  is a neural network. The difference is now that the weights and biases of  $\tau$  are not the output of an autoregressive conditioner network  $c$ ; instead, the parameters of the neural network are learned directly. In a B-NAF, the affine transformations  $L : \mathbb{R}^{ad} \rightarrow \mathbb{R}^{bd}$ , for  $a, b \in \mathbb{Z}^+$ , used at a given layer are always in a lower triangular block form

$$L(x) = \begin{pmatrix} u(B_{11}) & 0 & \dots & 0 \\ B_{21} & u(B_{22}) & \dots & 0 \\ \vdots & \vdots & \ddots & \vdots \\ B_{d1} & B_{d1} & \dots & u(B_{dd}) \end{pmatrix} x + \mu,$$

where  $u : \mathbb{R} \rightarrow \mathbb{R}^+$ , each  $B_{ii} \in \mathbb{R}^{a \times b}$  and  $\mu \in \mathbb{R}^{bd}$  is the freely parameterised bias term. The positivity-ensuring transform  $u$  enforces monotonicity. Bijectivity is further ensured by using bijective activation functions. Note that this particular form of affine transformation place restrictions on the structure of the neural network. For instance, the hidden dimensions must be a multiple of the input dimension  $d$ . Similarly to NAFs, B-NAFs also have a universality result.

For each synthetic test problem we used a single B-NAF with the tanh activation function and  $u(x) = \exp(x)$ . The B-NAF used had two hidden layers and was of the form

$$f_{BNAF} = L_3 \circ \tanh \circ L_2 \circ \tanh \circ L_1,$$

with lower triangular block affine transformations  $L_1 : \mathbb{R}^2 \rightarrow \mathbb{R}^{16}$ ,  $L_2 : \mathbb{R}^{16} \rightarrow \mathbb{R}^{16}$  and  $L_3 : \mathbb{R}^{16} \rightarrow \mathbb{R}^2$ . The B-NAF was initialised using the same default random initialisation in both the KSD and KLD experiments. 10,000 iterations of Adam were used, with learning rate 0.001.

**Polynomial (Cubic):** Polynomials were first put forward as possible parametric transport maps in measure transport [Marzouk et al., 2016, Parno and Marzouk, 2018]. In Marzouk et al. [2016], each component of a polynomial transport map  $T : \mathbb{R}^d \rightarrow \mathbb{R}^d$ , was parameterised as a linear basis expansion of multivariate polynomials  $\phi_j : \mathbb{R}^d \rightarrow \mathbb{R}$ . Each  $\phi_j$  is further parameterised with respect to a vector of polynomial degrees  $j = (j_1, \dots, j_d) \in \mathbb{N}^d$  as a product of  $d$  univariate polynomials of the form

$$\phi_j(x) = \prod_{k=1}^d \psi_{j_k}(x_k),$$

where each  $\psi_{j_k}(x_k)$  is a univariate degree  $j_k$  polynomial. These  $\psi_{j_k}$  can come from orthogonal families of polynomials or simply be monomials. For instance, we could take the  $\psi_{j_k}$  to be orthogonal with respect to the reference measure of the transport map. The  $i$ th component of  $T$  can thus be written as

$$T_i(x) = \sum_{j \in \mathcal{J}_i} \lambda_{j,i} \phi_j(x),$$

where each  $\lambda_{j,i} \in \mathbb{R}$ . This is a flexible parameterisation that can enforce triangularity through the choices of the  $\mathcal{J}_i$ . For example, a natural choice to enforce triangularity would be to take  $\mathcal{J}_i$  to consist of vectors  $j = (j_1, \dots, j_i, 0, \dots, 0)$  such that  $\sum_k j_k \leq p$ . The first constraint enforces triangularity and the second restraint ensures that the total degree of the resulting polynomials would be no greater than a given  $p \in \mathbb{N}$ . In higher dimensions, this may not be practical since the number of parameters grows quickly as the dimension increases. Thus other constraints on  $\mathcal{J}_i$  were put forward, such as removing mixed terms in the basis.

An issue with this approach is that the resulting maps are not monotonic for all values of the coefficients  $\lambda_{j,i}$ . In Marzouk et al. [2016] and Parno and Marzouk [2018], monotonicity was constrained locally at a given set of samples  $\{u_i\}_{i=1}^n$  from the reference distribution. Due to the triangular nature of the transport map, this effectively results in a finite set of linear constraints of the form  $\partial_{x_i} T_i(u_k) > 0$  for  $i = 1, \dots, d$  and  $k = 1, \dots, n$ . In our implementation of KLD-based polynomial transport for the synthetic test bed, we found that this approach was not necessary since, in each case, the resulting Jacobian always had a positive determinant.

In our synthetic experiments, we used the the natural choice of the  $\mathcal{J}_i$  that enforces triangularity that we previously discussed with  $p = 3$  and took the  $\psi_i$  as simple monomials. The overall transport map was thus a multivariate cubic polynomial of the form

$$\begin{pmatrix} T_1(x_1) \\ T_2(x_1, x_2) \end{pmatrix} = \begin{pmatrix} \sum_{i=0}^3 c_i x_1^i \\ \sum_{i=0}^3 \sum_{j=0}^{3-i} c_{ij} x_1^i x_2^j \end{pmatrix}.$$

The polynomial transport map was initialised to the identity in all synthetic experiments. 10,000 iterations of Adam were used, with learning rate 0.001.

**IAF mixture:** A mixture of transport maps is a distribution of the form

$$\sum_{i=1}^n w_i T_{\#}^{(i)} Q_i,$$

where the  $T^{(i)}$  are each a transport map of a given form, the  $Q_i$  are possibly distinct reference distributions and the mixing weights  $w_i \geq 0$  satisfy  $\sum_i w_i = 1$ . This is a very flexible extension to using just a single transport map. Furthermore, in principle, both the number of mixing components  $n$  and the mixing weights  $w_i$  could be learnt. For example, the weights  $w_i$  could be the output of a neural network with softmax applied to the output layer<sup>4</sup>, as was done in Pires and Figueiredo [2020].

For simplicity, in our synthetic experiments, we *a priori* set  $n = 4$  and further set each  $w_i = 1/4$ . We took each  $T^{(i)}$  as a single IAF, where the dimensionality of the hidden units in the single hidden layer was 8. Refer to our discussion of an IAF in Appendix B.2 or Kingma et al. [2016] for full details of an IAF. The  $Q_i$  were initialised as Gaussians with means  $(-2, 2), (-2, -2), (2, -2), (2, 2)$  respectively and each with identity covariance matrix. 30,000 iterations of Adam were used, with learning rate 0.001.

**ReLU network:** Refer to Definition 4 for the definition of a deep ReLU network.

For our synthetic experiments, we implemented a deep ReLU network for each synthetic test problem. When using KSD, the transport map need not be a diffeomorphism and so, to illustrate this flexibility, the input dimension of the ReLU network for each experiment was taken as 4 (while the dimension of the target was 2). For each problem, the ReLU network  $f_{ReLU} : \mathbb{R}^4 \rightarrow \mathbb{R}^2$  had two hidden layers and was of the form

$$f_{ReLU} = F_3 \circ \sigma \circ F_2 \circ \sigma \circ F_1,$$

where  $F_1 : \mathbb{R}^4 \rightarrow \mathbb{R}^{20}$ ,  $F_2 : \mathbb{R}^{20} \rightarrow \mathbb{R}^{20}$  and  $F_3 : \mathbb{R}^{20} \rightarrow \mathbb{R}^2$  are affine transformations and  $\sigma$  is the ReLU non-linearity, defined in Appendix A.4. Using the default random initialisation of these ReLU networks nearly always resulted in bad output. So, for each synthetic experiment, the ReLU network was pretrained for 10,000 iterations of KSD-based measure transport using Adam with learning rate 0.001, in order to approximate the reference distribution  $\mathcal{N}((0, 0), I_2)$ . That is, we pretrained the ReLU network in order to initialise it close to  $T_{\#}Q \approx \mathcal{N}((0, 0), I_2)$ . After pretraining, 50,000 further iterations of Adam were used for each synthetic test problem, with learning rate 0.001.

### B.3 Details of the Biochemical Oxygen Model Experiment

**Derivation of the Posterior:** Following on from Section 4.2, recall that the two-dimensional biochemical oxygen demand model is of the form

$$B(t) = \alpha_1(1 - \exp(-\alpha_2 t)).$$

Due to the positivity constraints on  $\alpha_1$  and  $\alpha_2$ , we perform inference on the log of the parameters and thus consider the model

$$B(t; \theta_1, \theta_2) = e^{\theta_1}(1 - \exp(-e^{\theta_2} t)).$$

---

<sup>4</sup>The  $i$ th component of the softmax function is of the form  $\text{softmax}(x)_i = \frac{\exp(x_i)}{\sum_j \exp(x_j)}$ .

Synthetic data  $y = (y_i)_{i=1}^6$  were generated at times  $t = 0, 1, 2, 3, 4, 5$  with the parameter values  $\theta_1 = \log(1)$  and  $\theta_2 = \log(0.1)$ , with observations corrupted by independent mean 0 Gaussian errors with variance  $\sigma^2 = 0.05^2$ . See Figure 6 for a plot of  $B(t; \theta_1, \theta_2)$  with these given parameter values alongside our generated synthetic data.

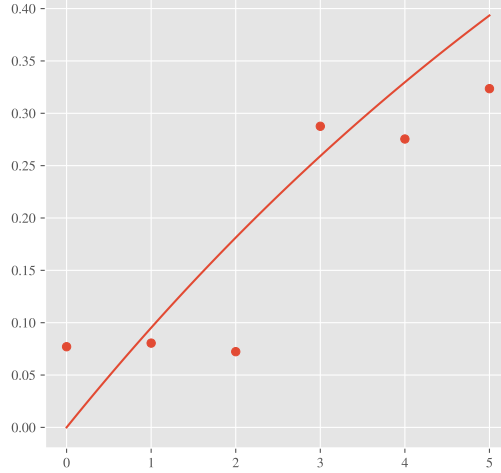


Figure 6: Plot of  $B(t; \log(1), \log(0.1))$  with the corresponding synthetic data at  $t = 0, 1, 2, 3, 4, 5$ .

The likelihood is thus of the form

$$p(y | \theta_1, \theta_2) = \prod_{i=1}^6 \mathcal{N}(y_i; B(t_i; \theta_1, \theta_2), \sigma^2),$$

The prior specified for  $\theta = (\theta_1, \theta_2)$  was  $\theta \sim \mathcal{N}((0, 0), I_2)$ . The resulting posterior density is thus of the form

$$p(\theta_1, \theta_2 | y) \propto \mathcal{N}(\theta_1, \theta_2; (0, 0), I_2) \prod_{i=1}^6 \mathcal{N}(y_i; B(t_i; \theta_1, \theta_2), \sigma^2).$$

**Methodology:** Our choice of parametric transport map was a Block Neural Autoregressive Flow (B-NAF) of Cao et al. [2019]. We used the same B-NAF as the one used in Section 4.1, where we again used a B-NAF with two hidden layers of the form

$$f_{BNAF} = L_3 \circ \tanh \circ L_2 \circ \tanh \circ L_1,$$

with lower triangular block affine transformations  $L_1 : \mathbb{R}^2 \rightarrow \mathbb{R}^{16}$ ,  $L_2 : \mathbb{R}^{16} \rightarrow \mathbb{R}^{16}$  and  $L_3 : \mathbb{R}^{16} \rightarrow \mathbb{R}^2$ . Refer to Appendix B.2 or to Cao et al. [2019] for a full description of a B-NAF. The lengthscale used for KSD was  $\ell = 0.1$ . We again used the Adam optimiser, with default learning rate 0.001 with 30,000 iterations for each method.

**Results:** See Figure 2 for samples obtained from each resulting transport map. The KSD-based method obtained a Wasserstein-1 distance of 0.069 and the KLD-based method obtained a Wasserstein-1 distance of 0.015. Refer to Appendix B.1 for details on how this was calculated. Figure 7 plots  $B(t; \theta_1, \theta_2)$  using samples from the prior and the approximate posterior using KSD-based measure transport.

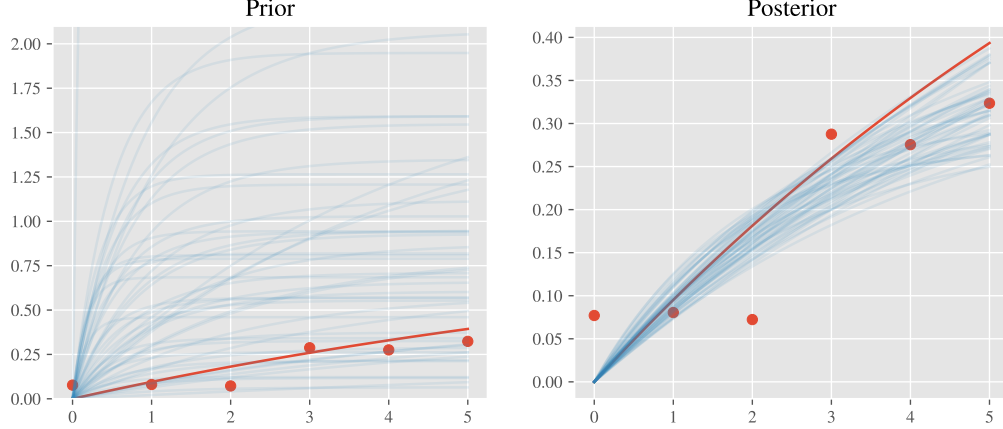


Figure 7: Plot of  $B(t; \theta_1, \theta_2)$  using 50 samples for  $\theta$  from (left) the prior and (right) the posterior, as approximated using KSD-based measure transport. The red line is  $B(t; \log(1), \log(0.1))$ .

## B.4 Details of the Generalised Lotka–Volterra Model Experiment

**Prior Specification:** Recall that, from Section 4.3, the generalised Lotka–Volterra model we considered was of the form

$$\begin{aligned}\frac{dp}{dt}(t) &= rp(t) \left(1 - \frac{p(t)}{k}\right) - s \frac{p(t)q(t)}{a + p(t)} \\ \frac{dq}{dt}(t) &= u \frac{p(t)q(t)}{a + p(t)} - vq(t),\end{aligned}$$

with parameters  $p_0, q_0, r, k, s, a, u, v > 0$ . These parameters are physical quantities, see Rockwood [2015] for their full meaning. Due to the positivity constraints on these parameter values, similar to our biochemical oxygen demand experiment Section 4.2, we again perform inference on the log of the parameters. We thus consider the model

$$\begin{aligned}\frac{dp}{dt}(t) &= e^{r'} p(t) \left(1 - \frac{p(t)}{e^{k'}}\right) - e^{s'} \frac{p(t)q(t)}{e^{a'} + p(t)} \\ \frac{dq}{dt}(t) &= e^{u'} \frac{p(t)q(t)}{e^{a'} + p(t)} - e^{v'} q(t),\end{aligned}$$

where we perform inference on the parameter  $\theta = (p'_0, q'_0, r', k', s', a', u', v') \in \mathbb{R}^8$ .

After an investigation of the sensitivities of the solutions of the ODE with respect to the parameter values, we specified the following independent prior

$$\begin{aligned} p'_0 &\sim \mathcal{N}(\log 45, 0.2^2), q'_0 \sim \mathcal{N}(\log 7, 0.3^2) \\ r' &\sim \mathcal{N}(\log 0.5, 0.3^2), k' \sim \mathcal{N}(\log 80, 0.15^2) \\ s' &\sim \mathcal{N}(\log 1.3, 0.2^2), a' \sim \mathcal{N}(\log 30, 0.1^2) \\ u' &\sim \mathcal{N}(\log 0.6, 0.1^2), v' \sim \mathcal{N}(\log 0.28, 0.07^2). \end{aligned}$$

Letting  $\mu \in \mathbb{R}^8$  be the vector of these given mean values and  $K$  the diagonal matrix with these given variances on the diagonal, we have  $\theta \sim \mathcal{N}(\mu, K)$ . This specification results in log-normal priors on the exponentiated parameters.

Synthetic data  $y = (p_i, q_i)_{i=1}^6$  were generated at times  $t = 0, 10, 20, 30, 40, 50$  with parameter values  $(p'_0, q'_0, r', k', s', a', u', v') = (\log 50, \log 5, \log 0.6, \log 90, \log 1.2, \log 25, \log 0.5, \log 0.3)$ ; these data were perturbed by independent mean 0 Gaussian errors with variance  $\sigma^2 = 40$ . See Figure 8 for a plot of the solution of the generalised Lotka-Volterra model with these given parameters alongside our generated synthetic data.

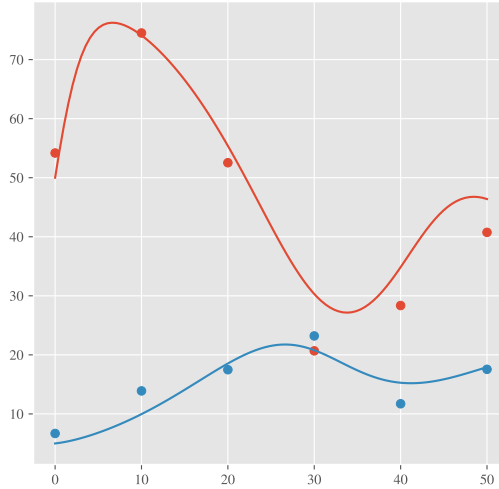


Figure 8: Solution of the generalised Lotka-Volterra model and the data that were provided at  $t = 0, 10, 20, 30, 40, 50$ .

The likelihood is thus of the form

$$p(y | \theta) = \prod_{i=1}^6 \mathcal{N}(p_i, q_i; (p_\theta(t_i), q_\theta(t_i)), \sigma^2 I_2),$$

where  $p_\theta(t), q_\theta(t)$  are the solutions of generalised Lotka-Volterra ODE (12) with given parameter  $\theta$ . The resulting posterior density is thus of the form

$$p(\theta | y) \propto \mathcal{N}(\theta; \mu, K) \prod_{i=1}^6 \mathcal{N}(p_i, q_i; (p_\theta(t_i), q_\theta(t_i)), \sigma^2 I_2).$$

**Methodology:** We used the `torchdiffeq` Python library [Chen et al., 2018] in order to numerically solve the Lotka–Volterra model and further utilised Pytorch’s automatic differentiation capabilities to propagate gradients through the solver. In our implementation, we used the default Dormand-Prince Runge-Kutta method. The reference measure used was the prior. Our choice of parametric transport map was a B-NAF with  $u(x) = \exp(x)$ , of the form

$$f_{BNAF} = L_3 \circ \tanh \circ L_2 \circ \tanh \circ L_1,$$

with lower triangular block affine transformations  $L_1 : \mathbb{R}^8 \rightarrow \mathbb{R}^{64}$ ,  $L_2 : \mathbb{R}^{64} \rightarrow \mathbb{R}^{64}$  and  $L_3 : \mathbb{R}^{64} \rightarrow \mathbb{R}^8$ . Refer to Appendix B.2 or to Cao et al. [2019] for a full description of a B-NAF.

For both the KSD and KLD experiments, we used the same random initialisation of the B-NAF and pretrained on 10,000 iterations of KLD-based measure transport on the prior (the reference measure), to ensure that the initial pushforward of samples through the B-NAF resulted in non-degenerate solutions of the Lotka–Volterra model.

The lengthscale used for KSD was  $\ell = 0.1$  and we again used the Adam optimiser, with default learning rate 0.001 with 50,000 iterations for each method.

**Results:** The KSD-based method obtained a Wasserstein-1 distance of 0.130, whereas the KLD-based method achieved a Wasserstein-1 distance of 0.110. Refer to Appendix B.1 for details on how this was calculated. The resulting approximating distributions for both the KSD and KLD methods are plotted in Figure 9.

## C Further Investigations

Here we report a series of further investigations, that explore specific aspects of KSD-based measure transport in more detail.

### C.1 Initialisation of Parameters in the Transport Map

Both KLD and KSD-based measure transport can be sensitive to the initialisation of the parameters in a given transport map. This is, for instance, evidenced in Figure 15. In our experiments we generally used a random initialisation as specified by their implementations in Pyro [Bingham et al., 2018]. In Appendix B, we specify for each experiment in the main paper what initialisation was used and whether we pretrained on the reference distribution  $Q$ .

A general remedy for poor initialisation is either to pretrain on the reference distribution. This was done in our applied examples in Section 4.2 and Section 4.3. Alternatively, in a Bayesian inference context one could pretrain on the prior distribution instead. The latter approach may be advantageous since we are guaranteed that the target’s support is contained within the prior’s support.

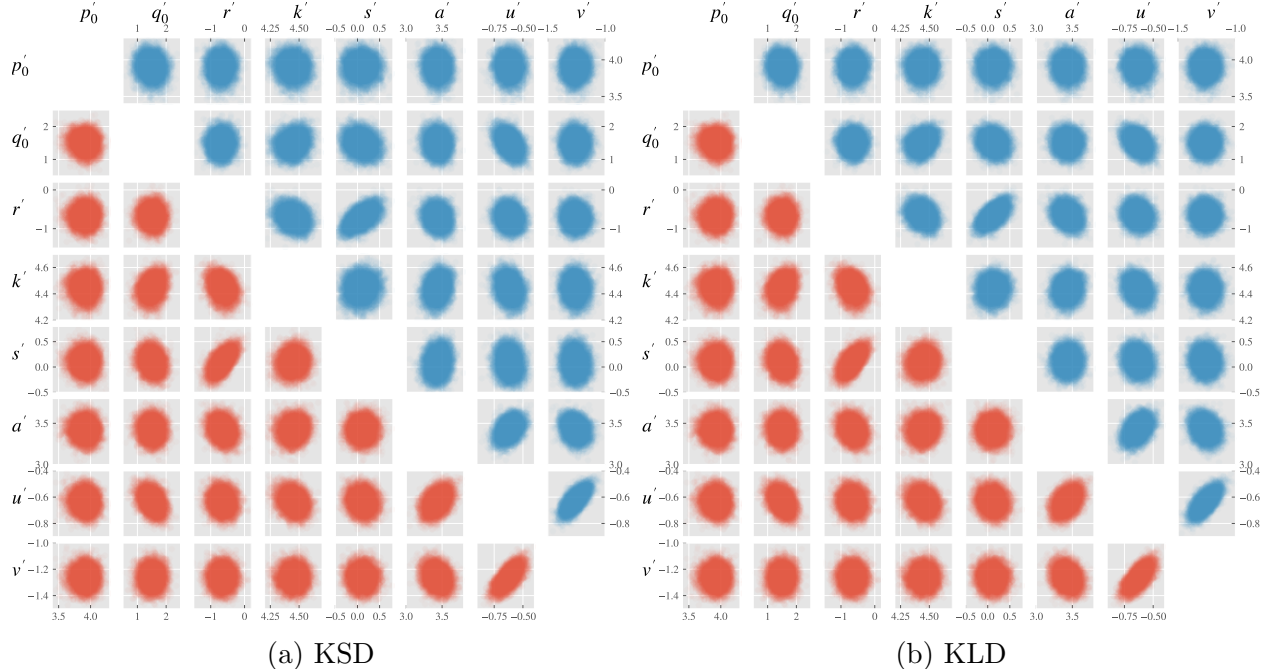


Figure 9: Two-dimensional projections of samples from (a) the KSD-based method and (b) the KLD-based method. In both plots, the lower triangular subplots are the two-dimensional projections of samples from the gold-standard HMC and the upper triangular subplots are the two-dimensional projections of samples from the two methods.

## C.2 Investigating the Choice of Stochastic Optimisation Method

In all our experiments in Section 4, we used the Adam optimiser of Kingma and Ba [2015] with a fixed batch size of 100 and with a varying number of iterations. In this section we explore how the output of KSD-based measure transport, with a fixed number of iterations of stochastic optimisation, interacts with the batch size as well as the stochastic optimisation method used. We fixed the target distribution as the multimodal problem and considered only B-NAF as our transport map with standard Gaussian reference distribution. Results are shown in Table 2, where we report the Wasserstein-1 distance using  $10^4$  samples (see Appendix B.1 for more details). We pretrained the B-NAF on the reference distribution using KLD as our loss for 5000 iterations of Adam with learning rate  $l = 0.001$ , hence the discrepancy with the main results reported in Table 1.

From Table 2, the most consistent and best performing optimisation methods were Adam and RMSprop, where the smaller learning rate of  $l = 0.001$  seemed to perform best. For stochastic gradient descent (SGD) and averaged stochastic gradient descent (ASGD), since the learning rate is non-adaptive, if the initial learning rate  $l$  is too large, the optimiser can fail to converge. This is evidenced by ASGD failing at a batch size of 25 with  $l = 0.005$  in Table 2. For each of the optimisation methods detailed in Table 2, all parameters other than the learning rate were set to their default values as specified in Pytorch.



Optimisation method	Batch size			
	25	50	100	200
Adam ( $l = 0.001$ )	0.594	0.546	0.121	<b>0.0827</b>
Adam ( $l = 0.01$ )	0.663	0.768	0.726	<b>0.242</b>
Adagrad ( $l = 0.001$ )	0.630	0.620	0.617	<b>0.616</b>
Adagrad ( $l = 0.01$ )	0.612	0.608	0.606	0.602
RMSprop ( $l = 0.001$ )	0.590	0.504	0.144	<b>0.0856</b>
RMSprop ( $l = 0.01$ )	1.00	0.699	<b>0.0653</b>	0.125
SGD ( $l = 0.001$ )	0.902	<b>0.194</b>	0.402	0.433
SGD ( $l = 0.005$ )	1.24	0.265	<b>0.143</b>	0.241
ASGD ( $l = 0.001$ )	0.701	<b>0.34</b>	0.401	0.432
ASGD ( $l = 0.005$ )	N/A	<b>0.166</b>	0.478	0.391

Table 2: The  $W_1$  distance to the multimodal target, varying the stochastic optimisation method. We used 10,000 iterations for each experiment. The  $l$  value next to the name of each optimisation method was the learning rate used. Bold values indicate which of the batch sizes obtained the best Wasserstein-1 distance for each given optimisation method. N/A values indicate when the optimisation method failed.

### C.3 Investigating the Effect of Quasi-Monte Carlo Sampling

To reduce the variance of the Monte-Carlo based gradient estimators, it was put forward in Buchholz et al. [2018] and Wenzel et al. [2018], to instead use randomised Quasi-Monte Carlo (QMC) in constructing an unbiased estimator of the gradient. This is achieved by simply replacing the Monte-Carlo samples from the base distribution with samples from a (randomised) QMC sequence in a principled manner. This may be especially useful in our setting, where the variance of the U-statistic estimator of KSD is often quite large. In this section, we explore the replacement of the Monte-Carlo based U-statistic estimator in Proposition 1 with a QMC-based estimator empirically. We first, however, briefly outline the rudimentary idea. Refer to Buchholz et al. [2018] and Wenzel et al. [2018] for the full detail.

A low-discrepancy sequence or a QMC sequence of a given length on  $[0, 1]^d$ , roughly speaking, allocates points such that the number of points in a given measurable subset of  $[0, 1]^d$  is proportional to its volume. A prototypical example of a randomised QMC estimator is the *random shift modulo 1*, where the sequence is generated by first specifying a grid of values  $x_i$  over  $[0, 1]^d$  and then sampling a  $u \sim U([0, 1]^d)$ , the resulting QMC sequence is the set of points  $x_i + u \bmod 1$ . Using an appropriate measurable function  $S : [0, 1]^d \rightarrow \mathbb{R}^d$ , one can use QMC to integrate with respect to a given distribution  $P$ , as long as  $S_{\#}U([0, 1]^d) = P$ , by pushing forward the QMC sequence through  $S$ . Figure 10 plots a randomly shifted (modulo 1) grid in two-dimensions, along with its pushforward on to the standard Gaussian against

a uniform sample.

Results are shown in Table 3, where we compare this prototypical QMC method with Monte Carlo; the convergence is shown in Figure 11. The transport map chosen was a NAF and of the same form as the NAF used in Section 4.1 and specified in Appendix B.2. We used 8000 iterations of Adam with learning rate 0.001. It appears that this QMC sequence generally performed worse than standard Monte-Carlo. These negative findings dissuaded us from further exploring QMC in this work. However, it remains to be seen whether more advanced randomised QMC sequences, such as the scrambled Sobol sequence that was used in Wenzel et al. [2018], provide performance gains relative to standard Monte Carlo.

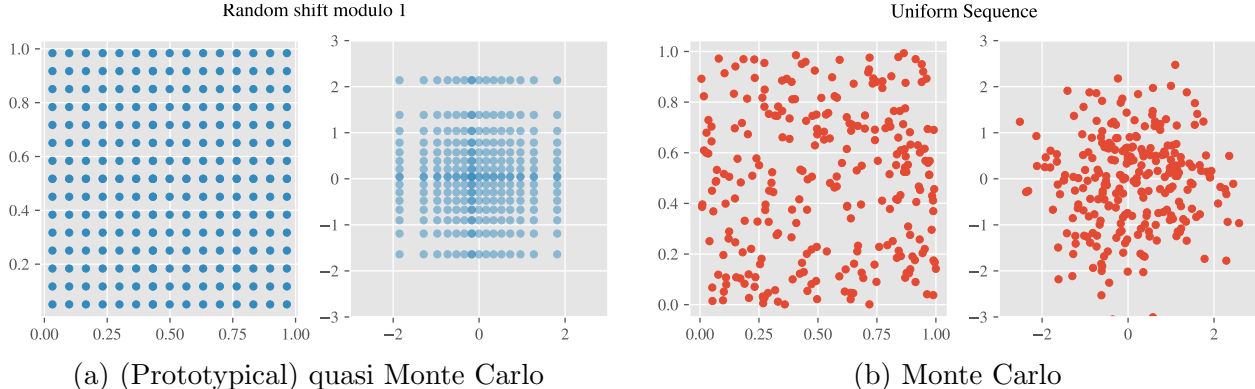


Figure 10: A size 256 quasi Monte Carlo point set (left) against a 256 length uniform sequence (right), each alongside their pushforwards to the standard Gaussian.

Sampling Method	Sinusoidal	Banana	Multimodal
Random shifted (modulo 1) grid	0.59	0.53	0.22
Monte Carlo	<b>0.55</b>	<b>0.39</b>	<b>0.16</b>

Table 3: The resulting  $W_1$  metrics from sampling using either quasi Monte Carlo or standard Monte Carlo. The transport map used was a NAF with 8000 iterations of Adam. Bold values indicate which sampling rule performed best on each target.

## C.4 Investigating the Choice of Reference Distribution

All the experiments in the main text used a Gaussian distribution as the reference distribution  $Q$ . However, different reference distributions could potentially offer some advantages, for instance in capturing thicker tails or multimodality [Izmailov et al., 2020]. To investigate, we used the IAF as our transport map and compared the following reference distributions: a mixture of two Gaussians, a symmetric multivariate Laplace distribution, and the standard Gaussian used in Section 4. The mixture of two Gaussians reference distribution was of the form  $\frac{1}{2}\mathcal{N}((0, -3), I_2) + \frac{1}{2}\mathcal{N}((0, 3), I_2)$ . The multivariate Laplace reference distribution was

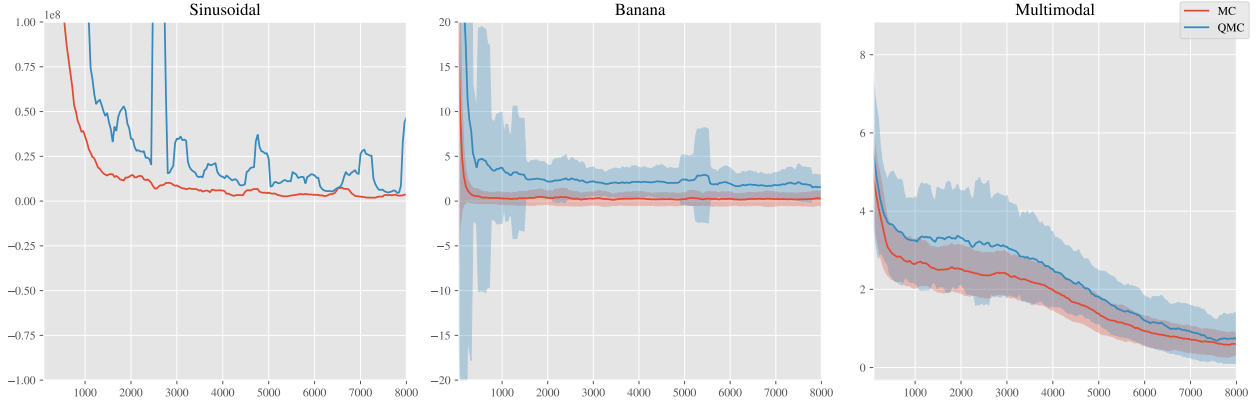


Figure 11: Loss function against number of iterations of Adam for standard Monte Carlo (MC) and quasi Monte Carlo (QMC).

of the form  $\text{Laplace}((0, 0), I_2)$ . The IAF we employed was the same one used in Section 4.1 and fully specified in Appendix B.2. For each experiment we used the Adam optimiser with learning 0.001 with 10,000 iterations of Adam. The target distributions were the synthetic distributions used in Section 4.1 and fully specified in Appendix B.2. Results are shown in Table 4 and notable output is shown in Figure 12.

Reference Distribution $Q$	Sinusoidal	Banana	Multimodal
Laplace	0.45	0.25	1.4
Gaussian Mixture	0.23	0.25	0.46
Gaussian	0.38	0.20	0.67

Table 4: The resulting  $W_1$  metrics from using different reference distributions  $Q$  in KSD-based measure transport for the targets in Section 4.1. The transport map used for each experiment was an IAF and was optimised with 10,000 iterations of Adam.

Looking at Figure 12, the heavier tails of the Laplace reference distribution resulted in heavier tailed output. Furthermore, the Gaussian mixture reference allowed the IAF to capture two modes, however it was unable to capture all four modes of the multimodal target. Results in Table 4 suggest it may be useful to consider the choice of  $Q$  as part of the optimisation problem to be solved, although we did not attempt to do so in this work.

## C.5 Investigating the Choice of Lengthscale

In this section, we investigate how the choice of lengthscale  $\ell$  of the inverse multi-quadric kernel (see Theorem 1) can affect the output of KSD-based measure transport. We will see that, relative to the target distribution, if  $\ell$  is too small the resulting output can be too focused if the target distribution has a relatively large dispersion, and on the other hand, if  $\ell$  is too large, the resulting output can exhibit pathologies. To demonstrate, we will focus

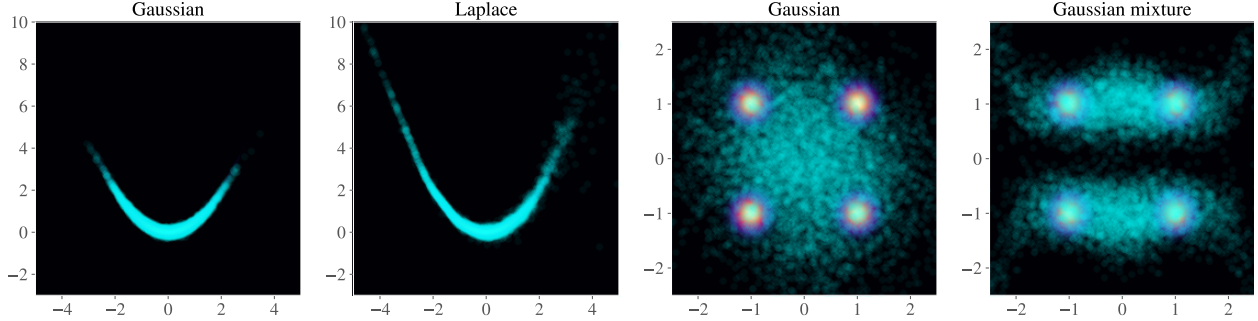


Figure 12: Output of KSD-based measure transport using different reference distributions on the banana and multimodal targets. The reference distribution used in each experiment is indicated in the titles of the corresponding subplots.

on the NAF transport map and consider simple Gaussian targets with covariance matrices  $10I_2$  and  $0.1I_2$ . We will demonstrate the pathologies also occur in a more complex example of the multimodal problem encountered in Section 4.1. Output is shown in Figure 13.

The NAF used is the same one used in the experiments in Section 4.1 and specified in Appendix B.2. We used the Adam optimiser for 10,000 iterations with learning rate 0.001.

## C.6 Investigating the effect of input dimension in the ReLU network transport map

In this section we investigate how changing input dimension of the ReLU network transport map can effect output. In order to isolate the input dimension as our variable of investigation, we fix the topology of the ReLU and consider ReLU networks of the form

$$f_{ReLU} = F_3 \circ \sigma \circ F_2 \circ \sigma \circ F_1,$$

where  $F_1 : \mathbb{R}^p \rightarrow \mathbb{R}^{20}$ ,  $F_2 : \mathbb{R}^{20} \rightarrow \mathbb{R}^{20}$  and  $F_3 : \mathbb{R}^{20} \rightarrow \mathbb{R}^2$  are affine transformations and  $\sigma$  is the ReLU non-linearity, defined in Appendix A.4. We consider input dimensions  $p = 1, 2, 3, 4, 5$ . The target we considered is the multimodal target of Section 4.1. For each experiment, we pretrained each ReLU network on the reference distribution  $\mathcal{N}((0, 0), I_2)$  for 10,000 iterations of Adam with learning rate 0.001. We then trained on the multimodal target for 20,000 iterations of Adam, again with learning rate 0.001. Due to the random effects of initialisation (see Figure 15), we ran the experiments for 10 different initialisations and report the best ones, see Table 5. The resulting transport maps are shown in Figure 14. As we can see, the transport map struggles with the multiple modes when the input dimension was  $p = 1$  or  $p = 2$ .

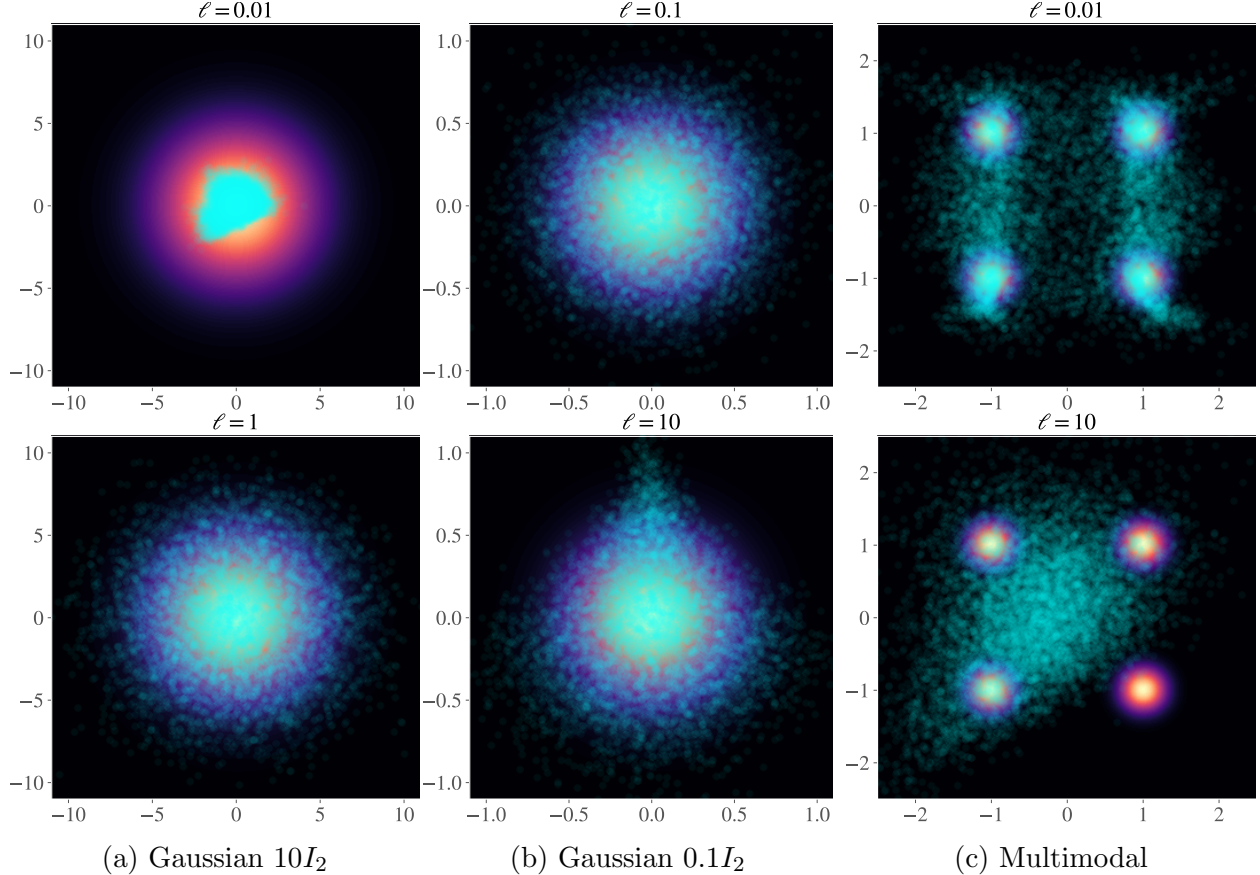


Figure 13: KSD-based measure transport with varying choices of lengthscale  $\ell$  for (a) a mean zero Gaussian target with covariance matrix  $10I_2$ , (b) a mean zero Gaussian target with covariance matrix  $0.1I_2$  and (c) the multimodal problem encountered in Section 4.1. The lengthscale  $\ell$  used in each experiment is indicated in the titles of the corresponding subplots.

Input dimension	$p = 1$	$p = 2$	$p = 3$	$p = 4$	$p = 5$
$W_1$	0.88	0.39	0.19	0.27	0.31

Table 5: The  $W_1$  distance to the target  $P$ , as a function of the dimension  $p$  of the reference distribution  $Q$ , using the ReLU neural network transport map.

## C.7 Investigating the Effect of the U-statistic estimator vs. the V-statistic estimator

Recall from Equation (5), that the square of KSD is of the form

$$\mathcal{D}_S(P, P')^2 = \mathbb{E}_{Y, Y' \sim P'} [u_p(Y, Y')],$$

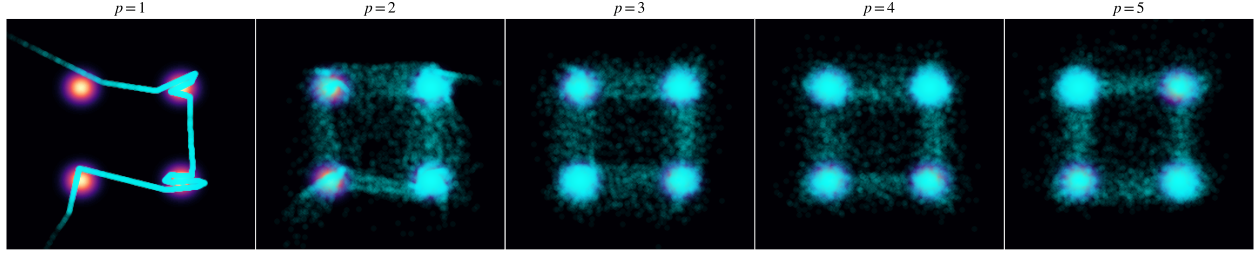


Figure 14: Output of KSD-based measure transport using the ReLU network transport with varying input dimension. The input dimension used in each experiment is indicated in the titles of the corresponding subplots.

where  $p$  is the density of  $P$ . For a given I.I.D. sample  $\{y_i\}_{i=1}^n$  from  $P'$ , there are two natural estimators of  $\mathcal{D}_S(P, P')^2$ . The first is the *V-statistic* (KSD-V),

$$\hat{\mathcal{D}}_S^V(P, P') = \frac{1}{n^2} \sum_{i=1}^n \sum_{j=1}^n u_p(y_i, y_j),$$

and the second is the *U-statistic* (KSD-U),

$$\hat{\mathcal{D}}_S^U(P, P') = \frac{1}{n(n-1)} \sum_{1 \leq i \neq j \leq n} u_p(y_i, y_j),$$

which is simply the V-statistic with the diagonal  $i = j$  elements removed. The advantage of U-statistic is that it is unbiased and, for any given sample, provides the minimum-variance unbiased estimator (MVUE) [Liu et al., 2016]. On the other hand, the V-statistic provides a non-negative estimator, due to the positive-definiteness of  $u_p$ .

To explore the differences between KSD-U and KSD-V as the objective, we re-ran the synthetic test bed experiments along with the majority of the transport maps in Section 4.1. Results are reported in Table 6. It appears that, although KSD-U and KSD-V often have very close outcomes, KSD-U seems to be strictly better than KSD-V. The transport maps and their initialisation were the same as was used in Section 4.1 and fully specified in Appendix B.2. For each experiment we used 10,000 iterations of Adam with learning rate 0.001.

## C.8 Pathologies of KSD for Measure Transport

Since KSD is a score-based method, it may exhibit similar pathologies to other score-based methods; see e.g. Wenliang [2020]. In this section, we detail certain pathologies of KSD-based measure transport that we found experimentally and, if available, offer potential mitigation strategies.

**Point Convergence:** For small batch sizes (e.g. 25) in the sinusoidal synthetic experiment of Section 4.1, it was observed (albeit rarely) that, when using the ReLU transport map, the

Transport Map	$N$	Sinusoidal		Banana		Multimodal	
		KSD-U	KSD-V	KSD-U	KSD-V	KSD-U	KSD-V
IAF	$10^4$	<b>0.38</b>	0.39	<b>0.20</b>	0.25	0.67	<b>0.61</b>
IAF (stable)	$10^4$	<b>0.35</b>	0.36	<b>0.16</b>	0.19	<b>0.61</b>	<b>0.61</b>
NAF	$10^4$	<b>0.55</b>	0.58	<b>0.39</b>	0.43	<b>0.095</b>	0.12
SAF	$10^4$	<b>0.23</b>	0.27	<b>0.20</b>	0.48	<b>0.30</b>	1.2
B-NAF	$10^4$	<b>0.78</b>	0.85	<b>0.70</b>	<b>0.70</b>	<b>1.0</b>	<b>1.0</b>
Polynomial (cubic)	$10^4$	<b>0.40</b>	0.61	<b>0.25</b>	0.41	0.51	<b>0.40</b>
IAF mixture	$3 \times 10^4$	<b>1.3</b>	<b>1.3</b>	<b>0.19</b>	0.39	<b>0.037</b>	0.040
ReLU network	$5 \times 10^4$	<b>0.71</b>	0.96	<b>0.43</b>	0.53	<b>0.22</b>	1.2

Table 6: Results from the synthetic test-bed using either the U-statistic (KSD-U) or V-statistic (KSD-V) form of KSD as our objective. The first column indicates with parametric class of transport maps was used; full details for each class can be found in Appendix B.2. A map-dependent number of iterations of stochastic optimisation,  $N$ , are reported - this is to ensure all the optimisers approximately converged. The table reports the Wasserstein-1 metric between the approximation  $T_{\#}Q$  and the target  $P$ . Bold values indicate which of KSD-U or KSD-V performed best for each transport map.

transport map converged to a limit in which all inputs were mapped to the origin. The origin is the mode of the sinusoidal synthetic density. This only occurred when using a degenerate initialisation and for small batch sizes. Due to the tightness of the sinusoidal target and the resulting large score values at points  $x$  diverging away slightly from the support of the target, the KSD value of output for all the transport maps used in Section 4.1 was generally of the order  $10^8$ . However, for the approximating transport map maps everything to the origin, the resulting KSD score was 200 with  $\ell = 0.1$ . Thus, from the perspective of KSD, a transport map that maps everything to the origin and thus having poor Wasserstein distance, was considered better than transport maps that obtain smaller Wasserstein distances.

This problem was mitigated by using better initialisations, larger batch sizes and pre-training on the reference distribution.

**Multimodal Failure:** It was found that, particularly with ReLU neural network transport map, the inferred transport map for the multimodal synthetic distribution in Section 4.1 could fail to find all four high density regions in the target. The outcome was highly dependent on the initialisation and even persisted when pretraining on the reference distribution. For example, in Figure 15 we plot three random initialisations of the ReLU transport map used in Section 4.1. Each transport map was pretrained on their reference distribution for 10,000 iterations of Adam. The KSD estimates with  $\ell = 0.1$  using 10,000 samples from the approximating distributions were 0.194, 0.205 and 0.147 from left to right respectively. The three outputs achieved broadly similar KSD scores, indicating that KSD was not able to differentiate between these outcomes. This problem is further exacerbated as the number

of modes of the target increases. For discussion of remedies, see Wenliang [2020].

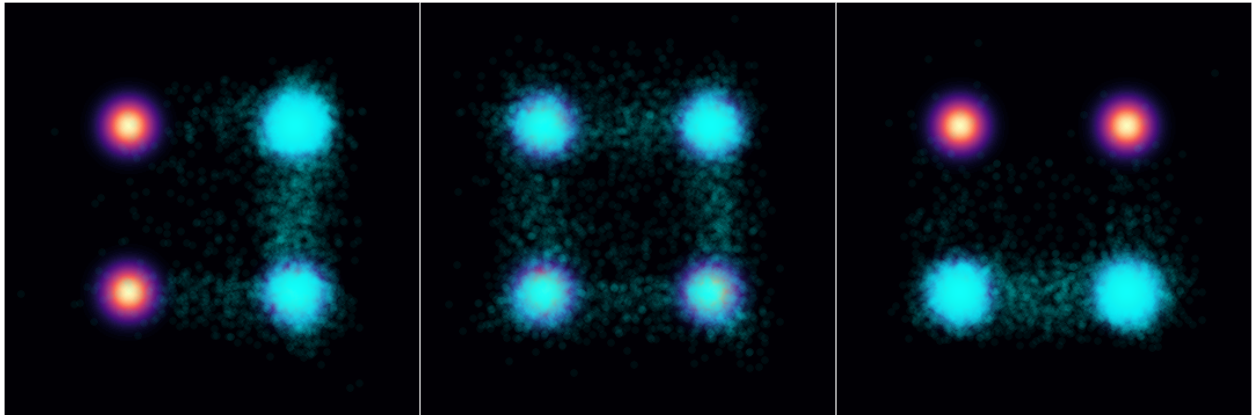


Figure 15: Output of KSD based measure transport with three random initialisations of the ReLU transport map. Each transport map was pretrained on their reference distribution for 10,000 iterations of Adam. The KSD estimates with  $\ell = 0.1$  using 10,000 samples from the approximating distributions were 0.194, 0.205 and 0.147 from left to right respectively.

**Poor Choice of Lengthscale:** Finally, as we have seen in Appendix C.5, if the choice of  $\ell$  is poor, the resulting output of KSD based measure transport can exhibit pathologies. This is demonstrated, for instance, in Figure 13. This issue is remedied by, for example, employing the median heuristic Garreau et al. [2018] to set the length-scale parameter in the kernel.